Advanced Powder Technology 29 (2018) 3107–3123

Contents lists available at ScienceDirect

Advanced Powder Technology

journal homepage: www.elsevier.com/locate/apt

Original Research Paper

Measuring the velocity fields of granular flows – Employment of a multi-pass two-dimensional particle image velocimetry (2D-PIV) approach

L. Sarno [a,*], A. Carravetta [b], Y.-C. Tai [c], R. Martino [b], M.N. Papa [a], C.-Y. Kuo [d]

[a] Dept. of Civil Engineering, University of Salerno, Via Giovanni Paolo II, 132, 84084 Fisciano, Italy
[b] Dept. of Civil, Architectural and Environmental Engineering, University of Napoli "Federico II", Via Claudio, 21, 80125 Napoli, Italy
[c] Dept. of Hydraulic and Ocean Engineering, National Cheng Kung University, Tainan City 701, Taiwan, ROC
[d] Research Center for Applied Sciences, Academia Sinica, Taipei 115, Taiwan, ROC

ARTICLE INFO

Article history:
Received 16 March 2018
Received in revised form 6 August 2018
Accepted 20 August 2018
Available online 31 August 2018

Keywords:
Particle image velocimetry
Granular flow
PIVlab
Granular temperature
Correlated velocity

ABSTRACT

Measuring velocity fields plays a crucial role in investigating the dynamics of granular flows, which can improve the modeling of hazardous geophysical flows (e.g. avalanches and debris flows) and the control of powder flows in industrial applications. Non-invasive optical methods are invaluable tools for estimating this physical quantity at the laboratory scale. Despite the recent improvements of particle image velocimetry (PIV) algorithms, the employment of PIV to granular flows is still a non-trivial application, where there are several specific aspects to be carefully addressed. Here, we address the main challenges of granular PIV applications and systematically test the open-source window deformation multi-pass code, PIVlab [Thielicke and Stamhuis, *J. Open Res. Soft.*, 2014], for dry granular flows in rotating drum and chute flow experiments. Three granular media (glass spheres, Ottawa sand and acetalic resin beads) with different optical properties are used as a broad test bench for validating the PIV approach. As well, comparisons between the estimations by PIVlab and those obtained by the commercial code, IDT ProVision-XS, are reported, where the advantages of the multi-pass approach are highlighted. This extensive experimental investigation allowed the evaluation of the accuracy of PIVlab in granular flow applications and also helped to assess the reliability of measurements of second-order statistics, such as the granular temperature. Finally, a guideline for setting a reliable PIV arrangement is suggested.

1. Introduction

Particle image velocimetry (PIV) has become a popular and effective tool in various fields of fluid mechanics, aerodynamics and hydraulic engineering (e.g. [58,1]). The classical PIV, consisting on two-dimensional investigations of the flow velocity field, is typically referred to as two-dimensional PIV (2D-PIV). More recent advances of the PIV approach involve tomographic PIV [12], plenoptic PIV [13] and light-field PIV [49,50]. The 2D-PIV technique is capable of finding the most probable velocities in predetermined subsets (typically called *interrogation windows* or *interrogation areas*) of a two-dimensional region of interest (ROI) of the flow domain. This task is achieved by determining the maximal value of the cross-correlation function of pairs of images, taken in a short time interval.

Classical PIV applications to transparent fluids require optically visible tracers and a laser sheet to illuminate them within a thin slice in the flow domain. The tracers have to be very small and roughly with the same density of the fluid under study, so that they flow with the fluid without noticeable velocity differences. Once these requirements are met, the tracers' velocities can be taken as reliable estimations of the flow velocities. The main errors of PIV are due to *loss-of-pair* and *gradient bias* (e.g. [46]). The first kind of error, typically due to a too small interrogation window compared to the magnitude of displacements, arises when the difference of the tracer numbers between the two images becomes too large and yields an increase of the background noise in the correlation. This error can be reduced by selecting an appropriate size of the interrogation window or by shortening the time interval between the images. The second error is caused by high shear in the interrogation window, which degrades the cross-correlation analysis by broadening the intensity peak. Generally, the precision of the PIV measurement can be improved when larger

* Corresponding author.
E-mail address: lsarno@unisa.it (L. Sarno).

https://doi.org/10.1016/j.apt.2018.08.014

interrogation windows are used, but large interrogation windows will decrease the measurement resolution (e.g. [57,18–19]).

More recently, PIV has been extended to dry granular flows, liquid-granular mixtures (e.g. [26,11,33,34,15,44]), silo discharge of granular materials [30,48], and soil deformation studies [57,3,18,19]. The dynamics of granular flows is a hot topic for the scientific community, as granular media are involved in several natural phenomena (e.g. debris flows and avalanches) (e.g. [51,25,31]) and engineering applications (e.g. conveyance and mixing of powders in industrial applications) (e.g. [3,30,48]). The application of a PIV approach to granular flows, often referred to as *granular PIV* or *g-PIV* [11], exhibits some peculiar traits. Although its working principle is identical to classical PIV, g-PIV differs in several aspects depending on the nature of the medium. Grains are typically non-transparent: thus seeding is generally not needed, as the grains themselves can be regarded as tracers (e.g. [33]). Yet, the grain opacity only allows measurements at the boundaries of the flow domain. The large size of grains (typically of order of mm) and the inability to investigate inside the flow domain render the use of laser sheets inadequate. Instead, the employment of alternative light sources, such as flash lights (e.g. [11,33]) or flickering-free LED lamps (e.g. [47,38,40]) is strongly encouraged. Another peculiarity of granular flows is that large shear may occur, especially in the presence of a no-slip basal condition (e.g. [24,22,44]). High shear may cause *gradient bias* errors in early PIV codes, especially if the optimization is performed by a zero-order matching algorithm assuming a rigid displacement in the interrogation window. Owing to such possible errors of PIV, the particle tracking velocimetry (PTV), another optical method based on tracking individual grains (e.g. [6,20,10]), was traditionally preferred to PIV despite its higher computational costs. Today, the aforementioned limitations of PIV seem to be surmounted by more robust algorithms, based on window displacement, multi-step and window deformation approaches (e.g. [56,45,46,53]). The main improvement of window displacement methods is the introduction of a relative shift of the interrogation window, in which the trial displacement is preliminarily calculated on a larger area. In the multi-pass approach this technique is iteratively applied on a sequence of progressively smaller interrogation areas. Such a refinement allows an increase of the spatial resolution without loss-of-pair errors for larger displacements. This approach is very effective to overcome the well-known trade-off of early PIV codes between spatial resolution and dynamic range, defined as the maximum range of measurable velocities. To limit the gradient-bias, the window deformation techniques employ higher order matching algorithms, which relax the aforementioned assumption of rigid displacement in the interrogation window and can be iteratively implemented within the aforementioned multi-pass algorithms. Such adaptive PIV methods iteratively adjust the size and shape of the individual interrogation windows so as to adapt to local flow gradient and seeding densities [17,18,19]. Another major challenge by g-PIV technique is the accuracy in estimating the second order statistics, such as the granular temperature (e.g. [20]). In fact, large errors may arise due to the spatial average of the PIV approach: that is, any PIV measurement is an averaged bulk measurement representative of the whole interrogation area and, thus, the grains' instantaneous velocities are subject to a smoothing. By statistical arguments and experimental verification Reynolds et al. [34] showed that the PIV spatial averaging errors typically cause an underestimation of the granular temperature, which increases with increasing size of the interrogation area. This underestimation is partly limited by the correlation of the instantaneous velocities from contiguous interrogation areas, due to auto-correlation of grains with themselves [34] and probably also due to correlated motion of grains on length scales larger than one grain diameter. All the aforementioned issues and peculiarities highlight that the g-PIV is still a non-standard and very challenging application.

Beside the commercial PIV codes, there are several open-source projects ongoing and becoming popular in the scientific community. In the present work we employed the free open-source code, PIVlab, developed by Thielicke and Stamhuis [53,54]. PIVlab is a Matlab code, based on state-of-the-art multi-pass window deformation algorithm. Under ideal conditions of synthetic images, where no noise and no shear exist, PIVlab is reported to provide rather accurate measurements with a random error typically smaller than 0.02 pixels/frame [52]. PIVlab has become very popular (e.g. [8,27,35]) since its first release in 2010, awarding more than 500 citations on Google Scholar. Also a few works on granular flows employed this code (e.g. [21,40,5,15,44]). However, to date the accuracy of PIVlab has not been thoroughly investigated in g-PIV applications.

In this work we studied the suitability of the multi-pass window deformation PIV approach to granular flows and, specifically, we assessed the accuracy of PIVlab. The specific objectives of this paper are: (a) to assess the accuracy of PIVlab in real g-PIV applications involving a wide range of granular materials with different optical properties (b) to select a reliable set of parameters for the PIV analysis; (c) to evaluate the quality of PIV estimations of the granular temperature.

Two standard experimental geometries, i.e. *rotating drum* and *chute flows* (G.D.R. [14]) and three kinds of granular media with different optical properties were investigated. The paper is composed of the following parts. The relevant aspects about g-PIV and the main features of PIVlab are summarized in Section 2. The experimental results are reported in Section 3. In particular, Section 3.1 reports the investigation in rotating drum where the absolute accuracy of PIVlab could be assessed by independent measurements of the rotating speed of the drum. Section 3.2 reports velocity measurements on chute flows of Ottawa sand, where a comparison between the measurements by PIVlab and those obtained by the commercial code IDT proVISION-XS is provided. Section 3.3 reports an investigation on white acetalic resin beads, whose challenging optical properties represent a further test bench for the PIV approach. General considerations about the PIV estimations of the granular temperatures are reported in Section 3.4. Finally, the conclusions are summarized in Section 4.

2. Pivlab and g-PIV applications

The main features of PIVlab, relevant to g-PIV, are here reported. Whenever necessary, the PIV theory is also recalled.

A 2D-PIV algorithm calculates the cross-correlation function of the image intensity field between two consecutive images, separated by a short time interval Δt. Each image is divided in partially overlapping regions, called interrogation windows (IW), where the cross-correlation function is evaluated. The maximization of this function allows determining the most likely displacement. The degree of overlap between contiguous IW is usually not larger than 50% of the size of IW. In fact, owing to Nyquist-Shannon sampling theorem, the spatial wavelength response has a cutoff at half the size of the IW (e.g. [58]). Let the interrogation plane be xy in a Cartesian coordinate system. With reference to a generic interrogation window, W, the zero-order cross-correlation optimization can be written as

$$\max_{\mathbf{d}} \int_W f_t(\mathbf{r}) f_{t+\Delta t}(\mathbf{r}+\mathbf{d})\, dA \tag{1}$$

where $\mathbf{d} \equiv (s_x, s_y)^T$ denotes the displacement vector with s_x and s_y being its x- and y- components, $\mathbf{r}$ is the position vector, f_t and $f_{t+\Delta t}$

are the grey intensities at time points t and $t+\Delta t$, respectively. In digital PIV applications (DPIV), (1) is rewritten in the discrete form

$$\max_{m,n}\left(\sum_{i,j=1}^{M} f_t(i,j) f_{t+\Delta t}(i+m, j+n)\right) \tag{2}$$

where M is the number of pixels in W, n and m are the discrete components of $\boldsymbol{d}$ in x- and y- directions. To speed-up the optimization (2), PIVlab is able to solve it in the frequency domain by using a Fast Fourier Transform (FFT). Sub-pixel accuracy is achieved by an interpolation algorithm. Specifically, PIVlab employs either a three-point Gaussian interpolation carried out separately in x- and y- directions, also referred to as 2×3 - point interpolation (e.g. [55]), or the more computationally expensive 9-point Gaussian interpolation. Clearly, a Gaussian interpolation is effective, as long as the cross-correlation function can be well described by a normal function around its peak. This approach is standard in classic 2D-PIV applications, especially when the seeders themselves show a Gaussian-like brightness intensity distribution, which typically leads to a Gaussian-like shape also of the cross-correlation peak. Conversely, to our knowledge there are no studies in literature specifically addressing whether a sub-pixel Gaussian interpolation is also suitable for g-PIV. Complementary image tests, reported in Appendix A, indicate that the correlation function typically exhibits a Gaussian-like shape around its peak for all the investigated granular media. Thus, Gaussian fit algorithms seem appropriate also in the context of granular PIV.

Since the optimization (1) (or (2) in its discrete form) is performed with respect to the sole unknown $\boldsymbol{d}$, i.e. it is assumed that the motion is rigid within W, *gradient-bias* errors arise if the flow is sheared. To limit such errors, more sophisticated matching algorithms allow that the displacement $\mathbf{d}(\mathbf{r})$ vary within W [46]: e.g. first-order algorithms assume that $\mathbf{d}(\mathbf{r})$ is linearly distributed around $\mathbf{r}_0 \in W$ by $\mathbf{d}(\mathbf{r}) \approx \mathbf{d}(\mathbf{r}_0) + \nabla\mathbf{d}|_0 \cdot (\mathbf{r}-\mathbf{r}_0)$. More refined window deformation algorithms implement different interpolation schemes using a higher number of points (e.g. [4]). Specifically, PIVlab employs a window deformation algorithm using 9 points. The trial displacements of the pixels in each IW can be estimated via either bilinear or spline interpolation. It is worth mentioning that this approach is particularly useful in g-PIV applications, where the shear rate may be large. In fact, though the method is more time-consuming and generally more sensitive to image noise due to the image interpolations, it helps reducing *gradient bias* errors. A sketch of the discretized interrogation plane with a 50% overlap and the 9-point window deformation technique, implemented in PIVlab, are shown in Fig. 1.

As mentioned in Section 1, another major error source, common to both classical PIV and g-PIV, is the *in-plane loss-of-pair*. To avoid it, a general recommendation is that IW should be at least

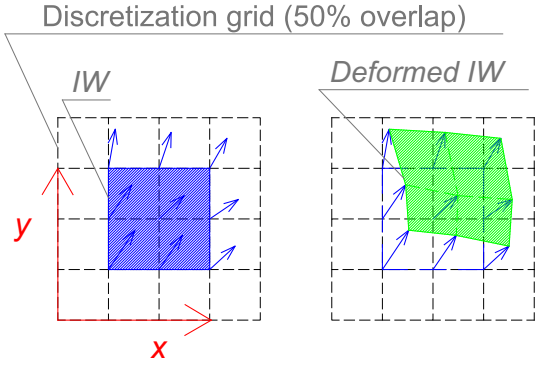

Fig. 1. Discretization of the interrogation plane (with 50% overlap of IW) and the 9-point window deformation technique using bilinear interpolation.

$4\times$ larger than the maximum $\mathbf{d}$ (e.g. [23]). Yet, for single pass PIV algorithms this requirement clearly limits the spatial resolution of measurements. Multi-pass algorithms overcome these issues allowing a progressive spatial refinement without loss of accuracy for large displacements. The multi-pass capability of PIVlab consists of a maximum of 4 passes and is implemented together with the aforementioned window deformation approach. That is, each PIV pass correlates the initial IW with the deformed one guessed by the previous PIV pass and, thus, determines the remaining displacement, which is added to the partial displacement by the previous pass (for more details see [53]).

The quality of a PIV analysis can be described by the signal-to-noise ratio (SNR), which can be estimated as the ratio between the first peak of the cross-correlation function and the second peak due to noise (e.g. [7]). A good exposure of the photographs and a suitable dynamic range of the camera sensor are necessary conditions for a good SNR. Furthermore, to achieve a reliable SNR, in classical 2D-PIV each IW should encompass a minimum amount of tracers: the optimal tracers' density has to be ≈5–10 per IW in classical applications on transparent fluids (e.g. [2]). This requirement can be met either by increasing the seeding density or by enlarging the IW. Gollin et al. [15] proposed to employ the same guideline also in g-PIV applications, where the tracers are replaced by grain particles. Yet, this requirement is rather stringent in g-PIV applications due to the large grain size and the impossibility of controlling the bulk density. Hence, its fulfillment typically amounts to choosing a very large IW, which limits the resolution of measurements. This requirement may be unnecessary, if the granular medium has sub-grain sized texture, i.e. an optical structure suitable for cross-correlation (e.g. [11]). In the present work we will show that, even if the grains do not exhibit clear sub-grain texture (e.g. glass spheres), a minimum number of particles in the IW should be guaranteed only in the 1st pass of the multi-pass PIV analysis. A short complementary analysis on the theoretical accuracy obtainable on semi-synthetic image pairs of granular media is given in Appendix B.

Beside the aforementioned errors also common to classical 2D-PIV applications, it is worth mentioning that dust spots within the ROI, occasional glares on grain surfaces or intermittent flicker of the light source could lead to a substantial deterioration of g-PIV analyses (e.g. [38]). Evidently these potential issues should be limited as much as possible at the stage of the experimental design. If they cannot be avoided at that stage, some image pre-processing before PIV analysis could be useful. To this regard, PIVlab allows different pre-processing strategies: e.g. contrast limited adaptive histogram equalization (CLAHE), Wiener filter, high-pass filter, intensity capping [53].

2.1. Estimation of second order statistics of the velocity field

Similar to turbulent flows, granular flows exhibit continuous fluctuations of the flow velocities, $\boldsymbol{u}'(t) = \boldsymbol{u}(t) - \bar{\boldsymbol{u}}$, around their Reynolds time-average, $\bar{\boldsymbol{u}} = 1/T\int_0^T \boldsymbol{u}(t)dt$. Major challenges arise when the PIV approach is also employed for estimating second-order statistics, such as the variance of $\boldsymbol{u}(t)$. Second-order measurements are tricky, as they involve a quadratic operator that, different from the average operator, does not dampen out the random errors of instantaneous velocities. Consequently, such errors cause noise in the estimated variance: e.g. a PIV typical random error of ≈0.02 pixel/frame would cause a noise floor of 0.02^2 pixel^2/frame. Another major error source, which conversely causes a systematic underestimation of the variance, is represented by the PIV spatial average in the interrogation window.

A useful second-order quantity, proportional to the specific kinetic energy of a granular flow and reminiscent of the thermody-

namic temperature, is represented by the granular temperature, T (e.g. [20]). The correct estimation of this quantity is crucial to study the granular flow regime. Considering the sole translational specific kinetic energy, for the sake of simplicity, T is given by

$$T = \frac{1}{3}\sum_{i=1}^{3}\left\langle (u'_i)^2 \right\rangle, \tag{3}$$

where u'_i is the i-component of $\boldsymbol{u}'(t)$ and $\langle\ \rangle$ is the ensemble average operator. Strictly speaking, the ensemble average in (3) should be evaluated over a large amount of repetitions of the same experiment. By assuming that the system under study is steady and ergodic, the ensemble averages in (3) can be approximated by the variances (in time) of the velocity within a single experiment: $\left\langle (u'_i)^2 \right\rangle \approx \sigma_i^2 = \overline{\left(u_i - \bar{u}_i\right)^2}$ (e.g. [44]). Reynolds et al. [34] showed that the true local granular temperature, T, related to a reference area small enough compared to the size of the grain particle, is higher than the PIV estimation, T^*, obtained from a IW n-times larger than such a reference area,

$$T^* \leqslant T \leqslant nT^* \tag{4}$$

The statistical arguments leading to (4) are briefly reported in Appendix C for the reader's interest. Under the hypothesis of no spatial correlation of contiguous instantaneous PIV measurements, (4) yields $T = nT^*$. Conversely, in case of full spatial correlation, $T = T^*$. Reynolds et al. [34] showed that a high spatial correlation arises on a length scale of one particle diameter, due to correlation of the particle with itself. Moreover, it has been speculated that correlated motion on larger length scales may arise, due to non-local rheological effects depending on the flow regime.

3. Experiments

Three kinds of experiments on free-surface steady flows, involving various granular media, are reported for validating the PIV approach. In all cases the measuring apparatus was composed of a high-speed digital camera and a flickering-free LED lamp. We did not carry out any pre-treatment of digital images, as preliminary tests revealed that the improvement was not significant in our dataset. The size of IWs and the number of PIV passes were systematically varied, so as to determine the most reliable PIV setting. Conversely, the following parameters were kept constant in all PIV analyses:

- the cross-correlation optimization is carried out in the frequency domain through FFT;
- the 9-point bilinear interpolation is used by the window deformation algorithm for the IW reconstruction;
- sub-pixel accuracy is achieved by 2×3 - point Gaussian interpolation;
- a 50% overlap of IW is employed at each PIV pass.

3.1. Experiments on glass spheres in a rotating drum

To investigate the accuracy of PIVlab, a series of experiments on a steadily rotating drum (e.g. G.D.R. [14]) were carried out at the National Chi Nan University (Taiwan). The clear advantage of this experimental setup is that the rotation speed of the drum could be controlled and independently assessed, so that the absolute accuracy of PIV measurements could be easily determined near the basal surface of the drum where a no-slip kinematic boundary condition (KBC) occurred. The rotating drum has an inner radius $R = 60$ cm, width $W = 10$ cm, and is powered by an electric motor. The rotation speed, Ω, could be adjusted by an inverter. The granular medium is composed of glass spheres of constant diameter $d = 2$ mm. To increase the quality of the PIV analysis, half of the number of the spheres was white and half black. The steady motion of the grains, induced by the drum rotation, was video-recorded at 2 kHz (i.e. 2000 fps) by a monochrome high-speed camera (mod. IDT X-Stream XS-3, 10-bit pixel depth and spatial resolution of 1280×1024 pixels), equipped with a lens of focal length 50 mm (mod. Sugitoh TSL-50095). So as to correctly capture the central zone of the flow, the camera was placed at a distance of ≈40 cm from the transparent wall of the drum and was centered at the section of the drum circumference where the tangent forms an angle of 41° with the horizontal. Depending on the resolution of the camera sensor, the distance between the camera and the object as well as the focal length of the lens, the spatial scale in the pictures is $1\,d \approx 19.5$ pixels, corresponding to 1 pixel ≈ 0.1026 mm. Given the scale and the frame rate, the theoretical random error of PIVlab would yield an ideal accuracy of ≈0.004 m/s. This investigation is meant to verify the real accuracy achievable. To get a proper exposure of the pictures, a flickering-free LED lamp (mod. 100 W-LED by U&U International Inc., ≈9000 lm) was employed, whilst the shutter time of the camera was set to 100 μs and the lens aperture to $f/2$. A sketch of the laboratory apparatus and an example picture of the ROI, a rectangle of size 3.2 cm × 8.4 cm in the xz plane, are shown in Fig. 2. A local Cartesian $Oxyz$ frame of reference, centered at the cross section under study, is considered. As shown by Fig. 2(c), the glossy surface of the grains does not exhibit a clearly visible sub-grain pattern, which renders this g-PIV application particularly challenging (cf. Appendices A and B). Different rotation speeds were investigated in a range between 1 and 5 revolutions per minute (rpm), from which two experiments were selected for PIV validation (Table 1). In this range of Ω a no-slip basal condition with no grain rolling was observed. Moreover, thanks to the resistances exerted by the side walls (e.g. [22,36,44]), a layer of grains with no deformation, spanning several grain diameters, was observed near the basal surface. Thus, the rotation speed of the drum, Ω, could be precisely assessed by measuring the linear velocity, $\hat{u}_x|_{z=d/2}$, of the lowest layer of spheres. To do it, individual spheres were manually tracked at $z = d/2$ over time intervals of 0.1–0.2 s taken from a larger interval, $\Delta t = 1s$, in the steady state. In order that the tracked particle was visible in both frames, the most suitable time interval (between 0.1 s and 0.2 s) was chosen depending on the rotation speed of the drum. The steadiness of the drum rotation is guaranteed by the servo-electric motor, so that a robust average of the rotation speed (reported in Table 1) could be obtained for each experiment. Such measurements exhibit an accuracy of order of $\approx 10^{-4}$ m/s, higher than the theoretical

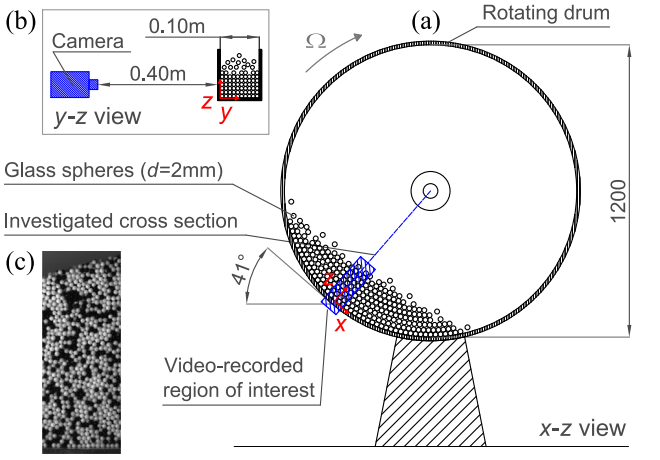

Fig. 2. (a) Sketch of the rotating drum, (b) Cross section (y-z view), (c) Example photograph of the ROI, centered at $x = 0$.

Table 1
List of experiments in the rotating drum, showing the rotation speed, Ω (in counter-clockwise notation), the flow depth, h, and the linear velocity, $\hat{u}_x|_{z=d/2}$, of the lowest layer of spheres determined by manual particle tracking.

Run	Ω[rpm]	h/d [m]	$\hat{u}_x\|_{z=d/2}$[m/s]	$\hat{u}_x\|_{z=d/2}$[px/frame]
Exp-1rpm	−1.044	37.5	−0.0655	−0.318
Exp−5rpm	−4.884	36.1	−0.3064	−1.487

PIV accuracy, and, thus, could be employed as reference for the PIV measurements.

In Table 1 $\hat{u}_x|_{z=d/2}$ is listed in both [m/s] and pixels/frame [px/frame] and also the time-averaged normalized flow depth, h/d, is reported. The same time interval $\Delta t = 1s$, in which Ω and h were estimated, was video-recorded and analyzed by PIVlab (ver. 1.41). The PIV analyses were performed on non-overlapping frame pairs (1–2, 3–4 etc.): thus, a sequence of 2000 pictures yielded 1000 instantaneous PIV measurements. A variety of analyses, using different numbers of PIV passes and IWs, were investigated (Table 2). In all the multi-pass analyses, reported here and hereafter, the spatial refinement from one pass to the next one was chosen ≤50% of the IW. In fact, it was preliminarily observed that a higher refinement leads to significant errors. The investigated PIV analyses are divided in two groups. In the first group, from PIVlab-1 to PIVlab-4, the effects of the multi-pass approach and of the spatial refinement were studied. In these analyses the IW size in the 1st pass was chosen equal to 40 pixels ≈ 2d, after preliminarily verifying that this length was larger than 4× the maximum displacement, so that loss-of-pair is avoided. In the second group, formed by PIVlab-4, PIVlab-5 and PIVlab-6, even larger IWs were investigated in the 1st pass.

So as to cancel out the rotation speed of the drum from the x-component velocity profiles, the relative velocity is employed

$$u'_x(z) = u_{x,measured}(z) - \Omega(R - z) \quad (5)$$

where $u_{x,\,measured}$ is the x-component of the PIV measurement in the fixed frame $Oxyz$. Fig. 3 shows the time-averaged profiles of u'_x and u_z. All the velocities, reported here and hereafter, are in standard dimensionless form obtained by dividing the dimensional values by $\sqrt{gd}$ (e.g. GDR [14]). To avoid overlaps with the u'_x profiles, the u_z profiles in Fig. 3 are shifted by the constant −0.5. Clearly, an accurate PIV analysis should be able to capture $u'_x \approx 0$ in the lower almost static zone, as well as $u_z \approx 0$ at the rigid bed where $\mathbf{u} \cdot \mathbf{n} = 0$.

Before studying the effects of the PIV setting, it can be noted by Fig. 3 that all u'_x profiles exhibit two regions with different behaviors: a lower zone with a very slow motion and an upper surface flow with larger values of u'_x. Such a stratified velocity profile, which was attempted to be described by a two-layer approach (e.g. [41,43]), is reported to occur also in different geometries such as chute flows with no-slip basal KBC (e.g. [24,25,44]). The same

Table 2
List of the PIVlab analyses in rotating drum experiments.

PIV analysis	Employed IWs	Overlap
PIVlab-1	Single pass, IW: 40 × 40 pixels	20 pixels (i.e. 2.05 mm ≈ 1d)
PIVlab-2	Two pass, IWs: 40 × 40, 20 × 20	10 pixels (i.e. 1.03 mm ≈ 0.5d)
PIVlab-3	Three pass, IWs: 40 × 40, 20 × 20; 10 × 10	5 pixels (i.e. 0.51 mm ≈ 0.25d)
PIVlab-4	Four pass, IWs: 40 × 40, 20 × 20; 10 × 10; 5 × 5	3 pixels (i.e. 0.31 mm ≈ 0.15d)
PIVlab-5	Four pass, IWs: 60 × 60, 30 × 30; 15 × 15; 8 × 8	4 pixels (i.e. 0.41 mm ≈ 0.20d)
PIVlab-6	Four pass, IWs: 80 × 80, 40 × 40; 20 × 20; 10 × 10	5 pixels (i.e. 0.51 mm ≈ 0.25d)

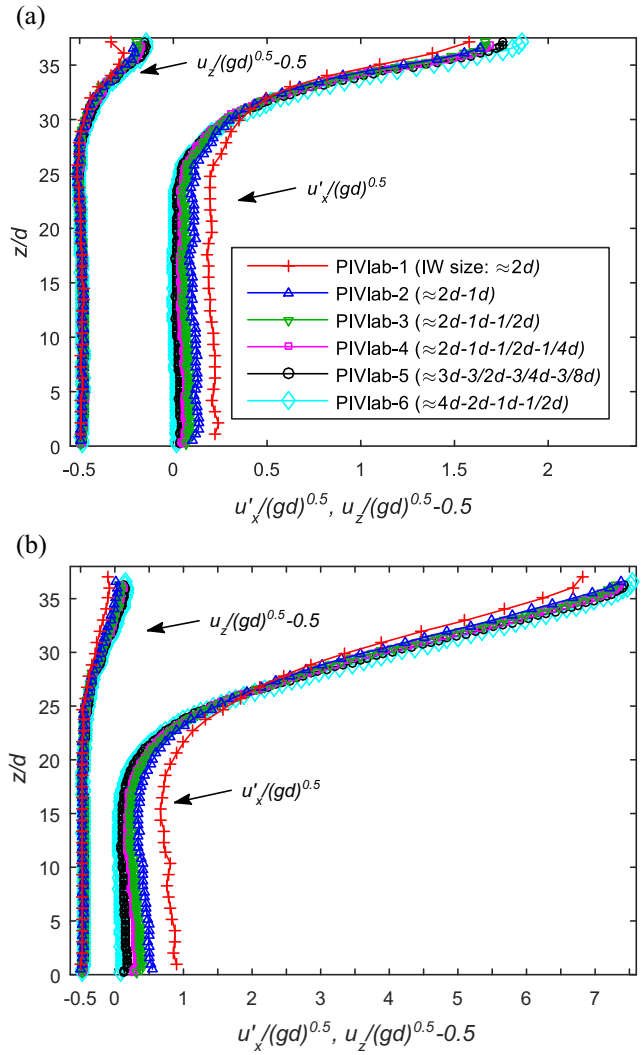

Fig. 3. Time-averaged velocity profiles, obtained by different PIV analyses. (a) Exp-1 rpm. (b) Exp-5 rpm. To avoid overlaps with the u'_x profiles, the u_z profiles are shifted by the constant −0.5.

shape was experimentally observed also by other measuring methods such as NMR and PTV (e.g. [28,20,9]). Thus, we can preliminarily conclude that PIVlab is capable of well capturing the shape of the velocity profile with a broad range of settings. Now, let us analyze the various PIV settings in detail. As the number of PIV passes decreases and, consequently, the IW size in the last pass increases, u'_x is noticeably underestimated, especially near the free surface, compared to more refined PIV analyses (e.g. cf. PIVlab-1 vs. PIVlab-4). This is due to the well-known underestimation of the displacements caused by the finite size of the IW and the consequent spatial average (e.g. [46]). Conversely, an evident overestimation of u'_x is found in the lower region, if coarser IWs are employed.

This finding is not in contradiction with that observed in the upper region. In fact, it should be noted that, before transformation (5), the PIV velocities were calculated in the fixed frame $Oxyz$ and are negative in this zone owing to the drum rotation. Hence, also in this region the employment of a coarser IW causes an underestimation of the absolute velocities. The differences become more subtle among the u'_x profiles obtained by using finer IWs in the last pass, indicating that an asymptotic profile is approached. Analogous remarks can be drawn by comparing the u_z profiles:

Table 3
Comparison of the time-averaged PIV measurements (in the fixed frame of reference *Oxyz*) nearest the basal surface ($z = z*$) and the reference linear velocities.

	PIV analysis	$z*/d$	$u_{x,measured}\|_{z*}$ [m/s]	$u_{x,measured}\|_{z*}$ [px/frame]	$\hat{u}_x\|_{z*}$ [m/s]	$\hat{u}_x\|_{z*}$ [px/frame]	$\Delta u_x\|_{z*}$ [m/s]	$\Delta u_x\|_{z*}$ [px/frame]
Exp-1rpm	PIVlab-1	1.03	−0.034	−0.167	−0.0654	−0.3173	0.0309	0.150
	PIVlab-2	0.52	−0.051	−0.249	−0.0655	−0.3178	0.0141	0.069
	PIVlab-3	0.26	−0.056	−0.271	−0.0655	−0.3181	0.0096	0.047
	PIVlab-4	0.15	−0.059	−0.285	−0.0656	−0.3182	0.0068	0.033
	PIVlab-5	0.21	−0.061	−0.296	−0.0656	−0.3181	0.0045	0.022
	PIVlab-6	0.26	−0.063	−0.307	−0.0655	−0.3181	0.0023	0.011
Exp-5rpm	PIVlab-1	1.03	−0.180	−0.874	−0.3058	−1.4840	0.1257	0.610
	PIVlab-2	0.52	−0.229	−1.111	−0.3063	−1.4866	0.0773	0.375
	PIVlab-3	0.26	−0.260	−1.262	−0.3066	−1.4879	0.0465	0.226
	PIVlab-4	0.15	−0.269	−1.306	−0.3067	−1.4884	0.0376	0.183
	PIVlab-5	0.21	−0.287	−1.392	−0.3067	−1.4881	0.0199	0.097
	PIVlab-6	0.26	−0.294	−1.429	−0.3066	−1.4879	0.0122	0.059

the maximum value of u_z nearest the free surface is better captured by the analyses with a spatial refinement of ≈1/2*d*-1/4*d*, while all PIV analyses accurately yield $u_z \approx 0$ in the lower region. These findings highlight the importance of the multi-pass approach, allowing the required spatial refinement without information loss for large displacements. Moreover, different from that suggested e.g. by Gollin et al. [15], it clearly emerges that the employment of a IW smaller than 1*d* in the last pass is feasible and also highly advisable for PIV accuracy. Yet, the spatial refinement alone is not sufficient to provide the best accuracy. In fact, from Fig. 3 it appears that even the most refined analysis, PIVlab-4, slightly overestimates u'_x in the lower almost static zone. The most accurate result at the bed is obtained by PIVlab-6, which uses a 1st pass IW of size ≈4*d* and, consequently, a coarser 4th pass IW (≈1/2*d*). Such a large IW in the 1st pass yields superior results probably due to the higher number of particles considered in the 1st cross-correlation. In this regard, the employment of a large enough IW in the 1st pass of a g-PIV analysis guarantees a minimum particle density, analogous to the well-known guideline for classical PIV indicating a tracer' density of ≈5–10 particles/IW [2]. Also the analysis PIVlab-5 with a 1st pass IW of ≈3*d* yields an estimation near the bed slightly better than PIVlab-4. In the light of these findings the employment of a IW of size ≈3*d*-4*d* in the 1st pass is advisable. Since the motion of the grains in the lower static zone is rigid with the drum, the time-averaged velocities, $u_{x,\,measured}|_{z\approx 0}$, estimated by PIV nearest the basal surface in the fixed frame *Oxyz*, could be quantitatively compared with the linear velocities of the drum independently measured. It is worth underlining that, owing to the PIV spatial discretization, the PIV measurements closest to the bed are located at a distance $z*$ from the bed equal to 50% of the IW size in the last pass. Thus, for an appropriate comparison also the reference linear velocity is calculated at the same $z*$ by $\hat{u}_x|_{z*} = \Omega(2\pi(R - z*))$. All the measurements, $u_{x,\,measured}|_{z*}$, are reported in Table 3 together with $\hat{u}_x|_{z*}$ and the error, $\Delta u_x|_{z*} = u_{x,measured}|_{z*} - \hat{u}_x|_{z*}$. According to that already observed, the best agreement is achieved by PIVlab-6, with errors of 0.011 and 0.059 pixel/frame for Exp-1rpm and Exp-5rpm, respectively. These errors are close to the PIVlab theoretical random error of ≈0.02 pixel/frame. Also PIVlab-4 and PIVlab-5 yield reasonably good results, while the errors by other PIV analyses rapidly increase with coarsening spatial resolution (up to 0.6 pixel/frame in the worst case of PIVlab-1).

Another crucial aspect to be investigated is the capability of the PIV approach of well estimating the granular temperature, *T*. Since u_y is inaccessible from the sidewall video recording, in this experimental setup, some assumption about σ_y^2 should be made. Following Jesuthasan et al. [20], here we assumed that $\sigma_y^2 \approx \sigma_z^2$. By also assuming the ergodicity of the system (cf. Section 2), the following formula will be employed here and hereafter

$$T(z) = \frac{1}{3}(\sigma_x^2 + 2\sigma_z^2) \tag{6}$$

The profiles of the dimensionless granular temperature, T/gd, are reported in Fig. 4. For all PIV calculations such profiles are strictly increasing with *z* and exhibit a roughly exponential shape in the moving layer, which is in good agreement with other measurements of *T* available in literature (e.g. [20,10,9]). As mentioned in Section 2, *T* is affected by two kinds of errors: (1) random errors propagated through the quadratic operator; (2) averaging errors,

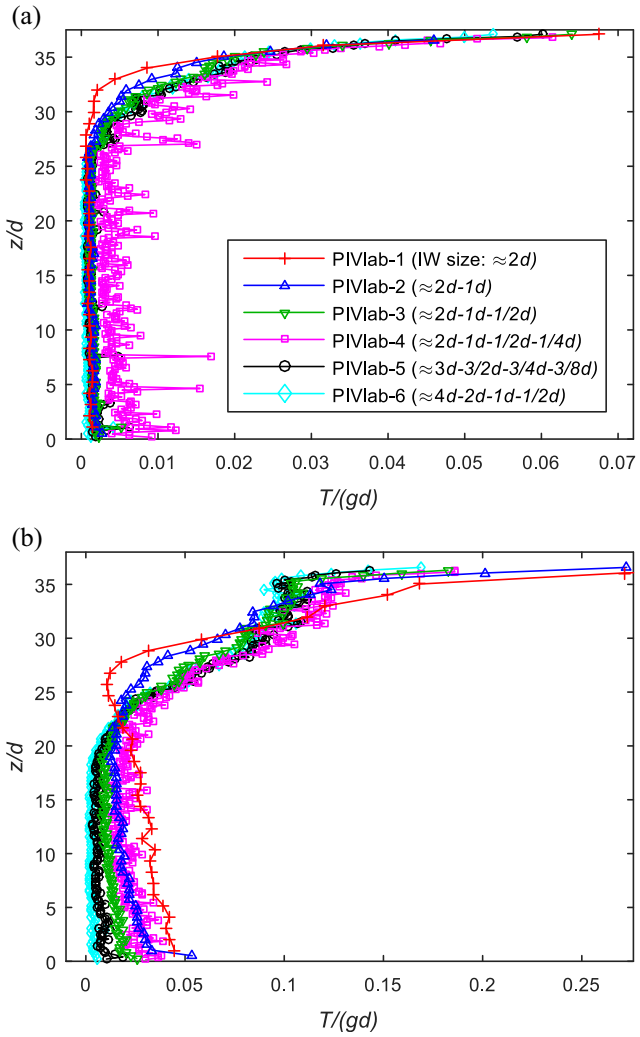

Fig. 4. Profiles of the granular temperature: (a) Exp-1rpm, (b) Exp-5rpm.

i.e. systematic underestimations due to PIV spatial averages. First of all, it is worth noting that the coarsest PIV analyses, PIVlab-1 and PIVlab-2, unrealistically overestimate T in the almost static lower region of Exp-5rpm (Fig. 4(b)). It reveals that for these analyses random errors prevail over averaging errors in the lower region. An analogous overestimation of T by PIVlab-1 and PIVlab-2 is also observed nearest the free surface of Exp-5rpm. Also in this case such a behavior is caused by the dominance of random errors over averaging errors, especially considering that PIV estimations obtained from coarse IWs are probably less accurate closest to the free surface, due to grain saltations.

Differently, in the rest of the profiles the general trend is that T slightly increases with the spatial refinement. This behavior is clearly due to decreasing averaging errors. However, it should be signaled that the rate of increase of T with the PIV spatial resolution is much lower than that predicted by (4) under the assumption of no-correlation of instantaneous velocities, and further decreases for IWs smaller than 1d. Thus, the mere employment of the amplification formula, $T = nT^*$, reported in Section 2, appears inappropriate for the investigated PIV spatial resolutions (≈2d-1/4d). These findings confirm that, according to the theory by Reynolds et al. [34], a high correlation exists in a neighborhood of ≈1d, due to the correlation of particles with themselves. On the other hand, in agreement with the experimental findings by Pouliquen [32], some correlated motion on length scales larger than ≈1d seems to occur in the investigated flow regime. These correlations are clearly beneficial for the accuracy attainable by PIV. These results suggest that a multi-pass PIV approach is capable of proper T estimations, as long as the size of the IW in the last pass is of order of ≈1d-1/2d. Moreover, it is reasonable to speculate that the most accurate estimation of T can be achieved by refining the IW as much as possible. Yet, the T profile calculated with the finest analysis, PIVlab-4, exhibits unphysical noise in the lower almost static region. Such a noise is clearly due to increasing random PIV errors, in turn caused by the low resolution of the camera sensor compared to the last-pass IW (5 pixels). We anticipate that also in the other experiments, performed on different granular media, we observed similarly noisy T profiles, if a IW of few pixels was employed in the last pass. Hence, it is clear that the maximum refinement, allowable for reliable T estimations, is limited by the camera resolution.

3.2. Chute flows of Ottawa sand

The second series of experiments concerned chute flows of Ottawa sand and was carried out at the National Cheng Kung University (Taiwan). Different from the previous investigation, no independent velocity measurements are available here. Conversely, the measurements by PIVlab could be compared with those obtained by the commercial PIV code, IDT ProVISION-XS (ver. 3.11). The laboratory apparatus is composed of a 140 cm-long Perspex flume with a rectangular cross section of width W = 4 cm and adjustable inclination. The upper part of the chute is used as reservoir and is connected to the lower part by a 5 cm-high gate located close to the bed. The granular material consists of Ottawa sand (ASTM C-778 20/30), a well-sorted round shaped silica sand with mean diameter $d = 7.25 \cdot 10^{-4}$ m and an angle of internal friction $\varphi \approx 34^\circ$ [51,38]. To improve the quality of PIV analysis, ≈10% of the sand was dyed with a black alcohol-based ink. For each run a constant amount of sand (≈6.7 kg) was loaded into the reservoir and, then, let flow down through the gate. In all experiments, the flow achieved the steady state for several seconds (e.g. [29,47]). A frame of reference $Oxyz$ with origin at the gate and x-axis parallel to the flume down-slope is considered. The steady flow was video-recorded by the same high-speed camera of Section 3.1. As well, the same camera parameters were used: frame rate of 2 kHz, shutter time of 100 μs, lens aperture of f/2. The camera was placed aside the chute at a distance of ≈25 cm from the side wall, centered at the cross section under study x = 20 cm.

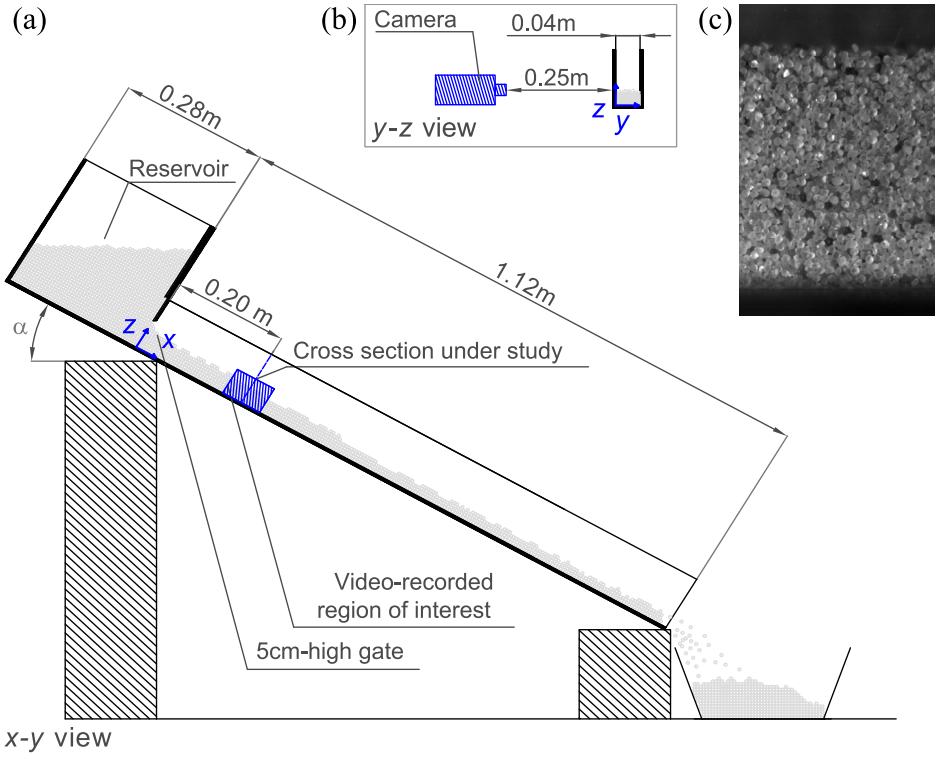

Fig. 5. (a) Sketch of the laboratory chute, (b) Cross section (y-z view), (c) Example picture of the ROI centered at x = 0.20 m.

Table 4
List of experiments of chute flows of Ottawa sand.

Run	α	h/d
Exp-28	28°	42.4
Exp-31	31°	34.0
Exp-34	34°	25.0
Exp-40	40°	20.9

The scale of the pictures is $1d \approx 11$ pixels, i.e. 1 pixel ≈ 0.0659 mm. The illumination of the ROI was guaranteed by the same LED lamp of Section 3.1, located aside the chute ≈30 cm far from the investigated cross section. A sketch of the apparatus is reported in Fig. 5. As shown in Fig. 5(c), the sand, different from glass spheres, exhibits a distinguishable sub-grain pattern, which is beneficial for the PIV analysis. Yet, some glares were occasionally observed on the grain surfaces. To reduce such glares, a thin film of paper was placed in front of the lamp with the result of slightly dampening the luminous flux.

Various inclination angles α were investigated so that various flow regimes, from quasi-static to dense collisional [14], could be observed. From the whole dataset, detailedly reported by Sarno [38], four experiments are selected here for PIV comparisons (Table 4). All PIV analyses are listed in Table 5. The first PIV analysis was carried out by using the commercial code, IDT ProVISION-XS,

Table 5
List of the PIV analyses on chute flows of Ottawa sand.

PIV Analysis	Employed interrogation windows	Overlap
IDT	Single pass, IW: 32 × 32 pixels	16 pixel (i.e. 1.06 mm ≈ 1.46d)
PIVlab-7	Single pass, IW: 32 × 32	16 pixel (i.e. 1.06 mm ≈ 1.46d)
PIVlab-8	Two pass, IWs: 32 × 32, 16 × 16	8 pixel (i.e. 0.53 mm ≈ 0.73d)
PIVlab-9	Three pass, IWs: 32 × 32, 16 × 16; 12 × 12	6 pixel (i.e. 0.40 mm ≈ 0.55d)
PIVlab-10	Four pass, IWs: 32 × 32, 16 × 16; 12 × 12, 6 × 6	3 pixel (i.e. 0.20 mm ≈ 0.27d)

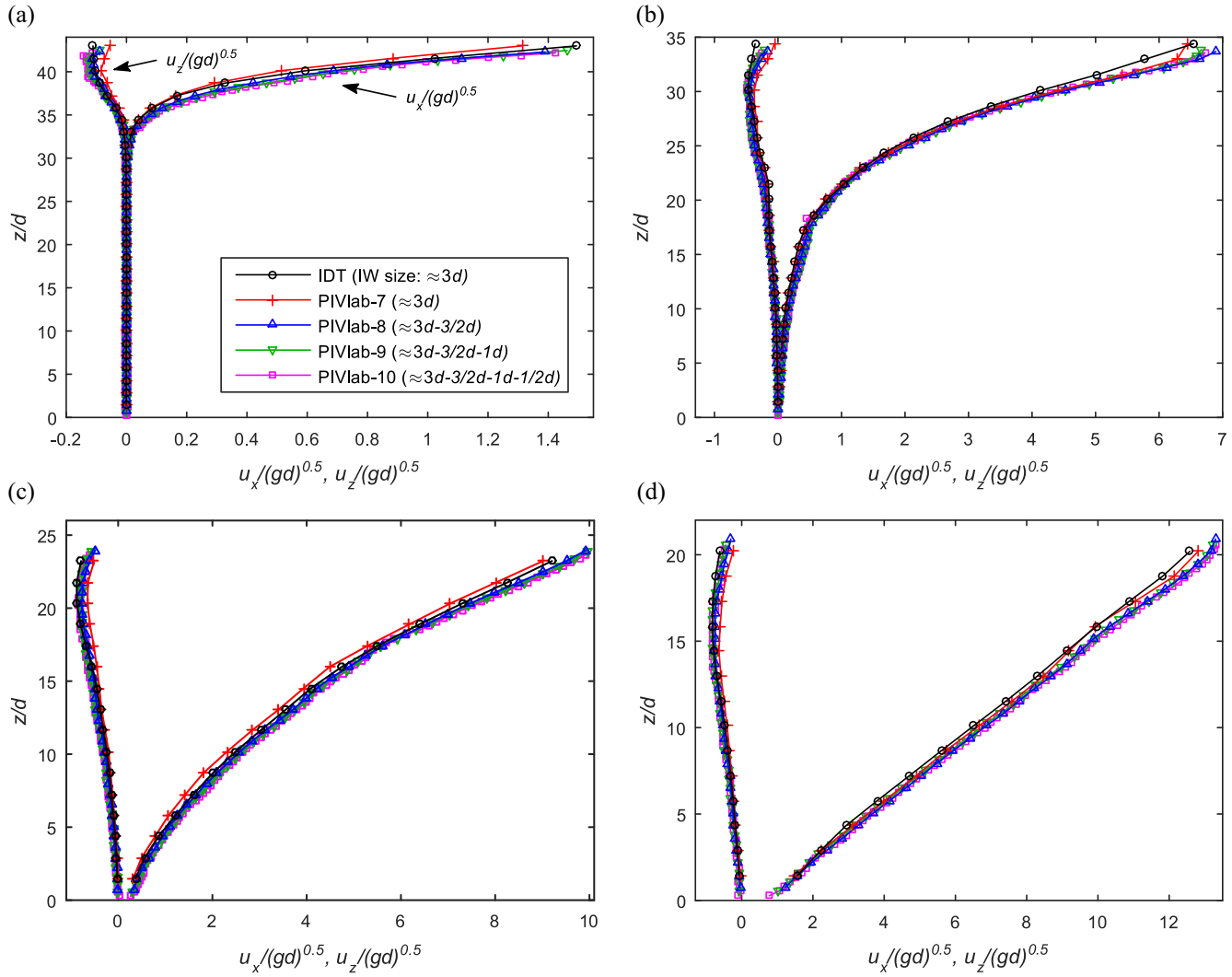

Fig. 6. Time-averaged velocity profiles, obtained by different PIV analyses a. Exp-28, (b) Exp-31, (c) Exp-34, (d) Exp-40.

where a standard single pass cross-correlation is employed. Since the bulk density of the granular medium varies in time, i.e. the granular flow cannot be regarded as incompressible fluid, the validation algorithm of the IDT code, exploiting the density-preserving assumption, was cautiously disabled (for more details see [16]). Analogous to the previous investigation, a sequence of 2000 frames, from a time interval of 1 s in the steady state, was analyzed. All the analyses employed a 1st pass IW of size 32 pixels $\approx 3d$. This size was preliminarily verified to be $\approx 4\times$ the maximum displacement, so that loss-of-pair issues are avoided. Due to the small size of the sand grains and the resolution of the camera sensor, the highest PIV refinement achievable here was only $\approx 1/2d$ (PIVlab-10). The time-averaged velocity profiles are reported in Fig. 6. Before proceeding to comparisons, it is worth noting that u_x exhibit various shapes depending on the flow regime, which are in sound agreement with that observed by Sarno et al. [44] on similar chute flows. In the runs with small inclination angle and high flow depth (Exp-28 and Exp-31), analogous to that observed in rotating drum, a stratified profile with a lower exponential tail occurs. As the chute inclination increases, the lower exponential tail gradually fades out (Exp-34) till the u_x profile becomes approximately linear (Exp-40). All the PIV analyses, including the one by IDT, capture the same trend of u_x and also $u_z \approx 0$ at the bed is correctly described.

Minor discrepancies among different PIV analyses are observed along the flow depth, especially near the free surface, where the flow velocities are larger and more difficult to be measured due to grain saltations. The general trend of all the analyses is substantially analogous to that already found in rotating drum experiments: a systematic underestimation of both $|u_x|$ and $|u_z|$ is observed if a coarser IW is employed in the last pass (e.g. PIVlab-7 vs. PIVlab-10). Yet, it should be noted that the discrepancies between different PIV analyses (especially as regards the most refined ones) are smaller than those observed on glass spheres, which is probably due to the better optical properties of Ottawa sand (cf. Appendices A and B). The PIV calculation, IDT, obtained by the commercial code IDT proVISION-XS, performs very similarly to PIVlab-7, carried out with the same PIV settings (i.e. single-pass and IW size of 32 pixels). Conversely, the multi-pass PIVlab analyses (PIVlab-8, PIVlab-9 and PIVlab-10) seem capable of delivering better estimations of the flow velocities, thanks to the higher spatial resolution and consequently smaller averaging errors. It especially holds closest to the free surface, where the velocity fluctuations due to grain saltations can be well-captured only by using a PIV spatial resolution equal or finer than $\approx 1d$.

Though in this experimental campaign we could not compare the PIV measurements with independent velocity measurements, in the light of the previous results in rotating drum and of the complementary tests reported in Appendix B, it is reasonable to speculate that the finest analysis PIVlab-10 yields the best time-averaged velocity estimations along the entire flow depth, h. Hence, the ℓ^2-norm of the velocity differences, $\| \Delta u \|_2 = \left((\Delta u_x)^2 + (\Delta u_z)^2 \right)^{1/2}$, were calculated for the various PIV analyses with respect to PIVlab-10.

As an example, the $\| \Delta u \|_2$ profiles, related to the runs Exp-28 and Exp-40, are reported in Fig. 7 in px/frame units, so as to ease comparisons with other experiments employing different camera settings. Fig. 7 shows that, while the lower slowly moving region is equally captured by all PIV analyses, larger differences occur near the free surface, where the flow velocities are larger. In agreement with the findings in rotating drum, $\| \Delta u \|_2$ increases with increasing size of the IW in the last pass. The depth averages of $\| \Delta u \|_2$ along h are summarized in Table 6 for all runs. The fact that for coarse analyses (IDT and PIVlab-7) such values are much larger than the random error of PIVlab under ideal conditions (0.02 pixel/frame) further highlights the importance of the multi-pass approach which allows the proper spatial refinement. On the other hand, the averaged $\| \Delta u \|_2$ for the finer analysis, PIVlab-9, is very small ($\approx$0.01–0.05 pixel/frame), suggesting that a PIV resolution of $\approx 1d$ is probably adequate for getting reliable estimations of the time-averaged velocities.

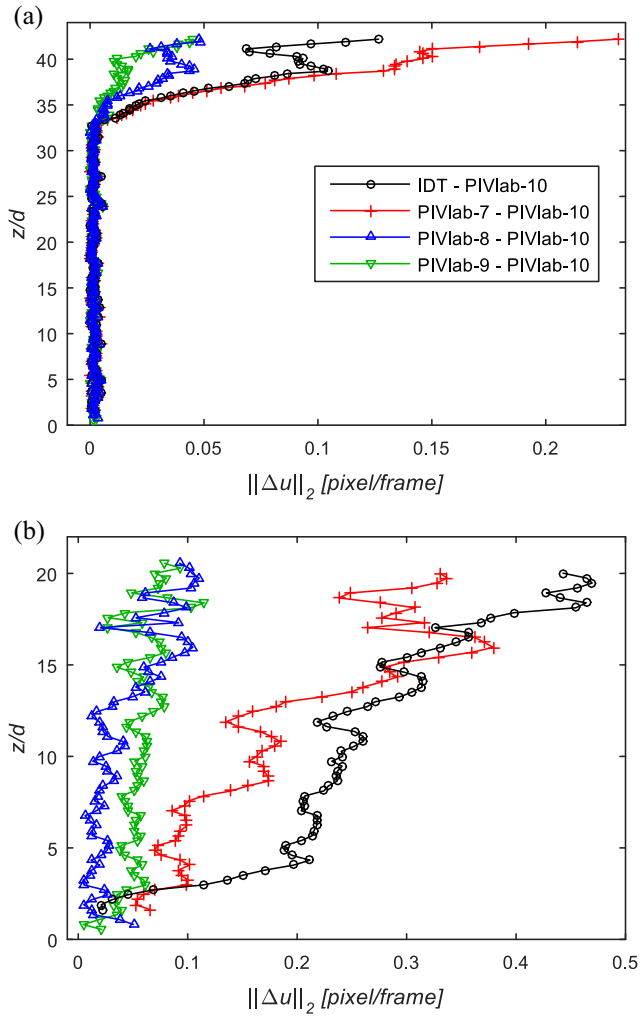

Fig. 7. ℓ^2-norm of the velocity differences, $\| \Delta u \|_2 = \left((\Delta u_x)^2 + (\Delta u_z)^2 \right)^{1/2}$, calculated with respect to the most refined analysis, PIVlab-10: (a) Exp-28, (b) Exp-40.

Table 6
Depth averages of $\| \Delta u \|_2 = \left((\Delta u_x)^2 + (\Delta u_z)^2 \right)^{1/2}$, calculated with respect to the most refined analysis, PIVlab-10.

	PIV analysis	Avg. $\| \Delta u \|_2$ [px/frame]	Avg. $\| \Delta u \|_2$ [m/s]
Exp-28	IDT	0.0152	0.0020
	PIVlab-7	0.0220	0.0029
	PIVlab-8	0.0070	0.0009
	PIVlab-9	0.0046	0.0006
Exp-31	IDT	0.0890	0.0116
	PIVlab-7	0.0527	0.0068
	PIVlab-8	0.0237	0.0031
	PIVlab-9	0.0134	0.0017
Exp-34	IDT	0.1362	0.0179
	PIVlab-7	0.2593	0.0341
	PIVlab-8	0.0641	0.0084
	PIVlab-9	0.0334	0.0044
Exp-40	IDT	0.2599	0.0340
	PIVlab-7	0.1884	0.0246
	PIVlab-8	0.0432	0.0056
	PIVlab-9	0.0557	0.0073

Similar to the previous investigation, let us proceed now to discuss the granular temperatures profiles, obtained by different PIV analyses (Fig. 8). Firstly, Fig. 8 shows that the T profiles of experiments Exp-28 and Exp-31 are very similar to those already found in the rotating drum geometry. Differently, in Exp-34 and Exp-40, characterized by a different flow regime (cf. Fig. 6) a slightly different shape is observed. As expected, the T profiles by PIVlab-7 and IDT, employing the same IW, are very similar and exhibit the lowest values among all the PIV analyses, clearly due to averaging errors. Yet, some discrepancies between these two T profiles arise in Exp-34 and Exp-40, where the estimations by PIVlab-7 are higher than those by IDT. This behavior is probably due to slightly larger random errors of the open source code compared to the commercial code. As regards the other profiles, in agreement with that observed in Section 3.1, it is found that T generally increases when the IW in the last pass is refined (e.g. cf. PIVlab-7 vs. PIVlab-8). This trend confirms the dominance of the PIV averaging errors over random errors, and is only occasionally reversed near the free surface (e.g. Exp-31), where larger random errors due the fluctuation of the free surface affect the coarse PIV analyses more than the fine ones. Nonetheless, analogous to that observed in Section 3.1, such an increase of T is rather weak, indicating strong correlation of the instantaneous velocities in the range of investigated IWs ($\approx 0.5d$-$3d$). Finally, it is evident from Fig. 8 that the T profile, obtained by the most refined analysis, PIVlab-10, exhibits some noise. This behavior, analogous to that already observed in the previous experimental campaign (cf. PIVlab-4), is due to random errors and is clearly unphysical, especially considering that in the lower almost static region of Exp-28 the fluctuation velocities are certainly very small. Once again, it is evident that the culprit of this noise is the extreme smallness of the IW (6 pixels in this case) compared to the resolution of the camera sensor. In the light of these findings on Ottawa sand, the smallest allowable IW size seems to be somehow greater than 6 pixels. Interestingly, this lower limit for the PIV resolution, in agreement with that found in the previous investigation, seems to be independent from the size and the optical properties of the granular material.

3.3. Chute flow of acetalic copolymer (POM) beads

In order to test the PIV approach under various experimental conditions, a further campaign on chute flow, carried out at the University of Salerno (Italy), is reported. In this section the computation time required by PIVlab, which depends on the number of PIV passes and on the IW sizes, is briefly discussed. The flume is analogous to that reported in Section 3.2, while the granular material was chosen intentionally different. The apparatus, identical to that employed by Sarno et al. [44], consists of a 2 m-long Perspex chute with a 8 cm-wide cross section and has an inclination angle

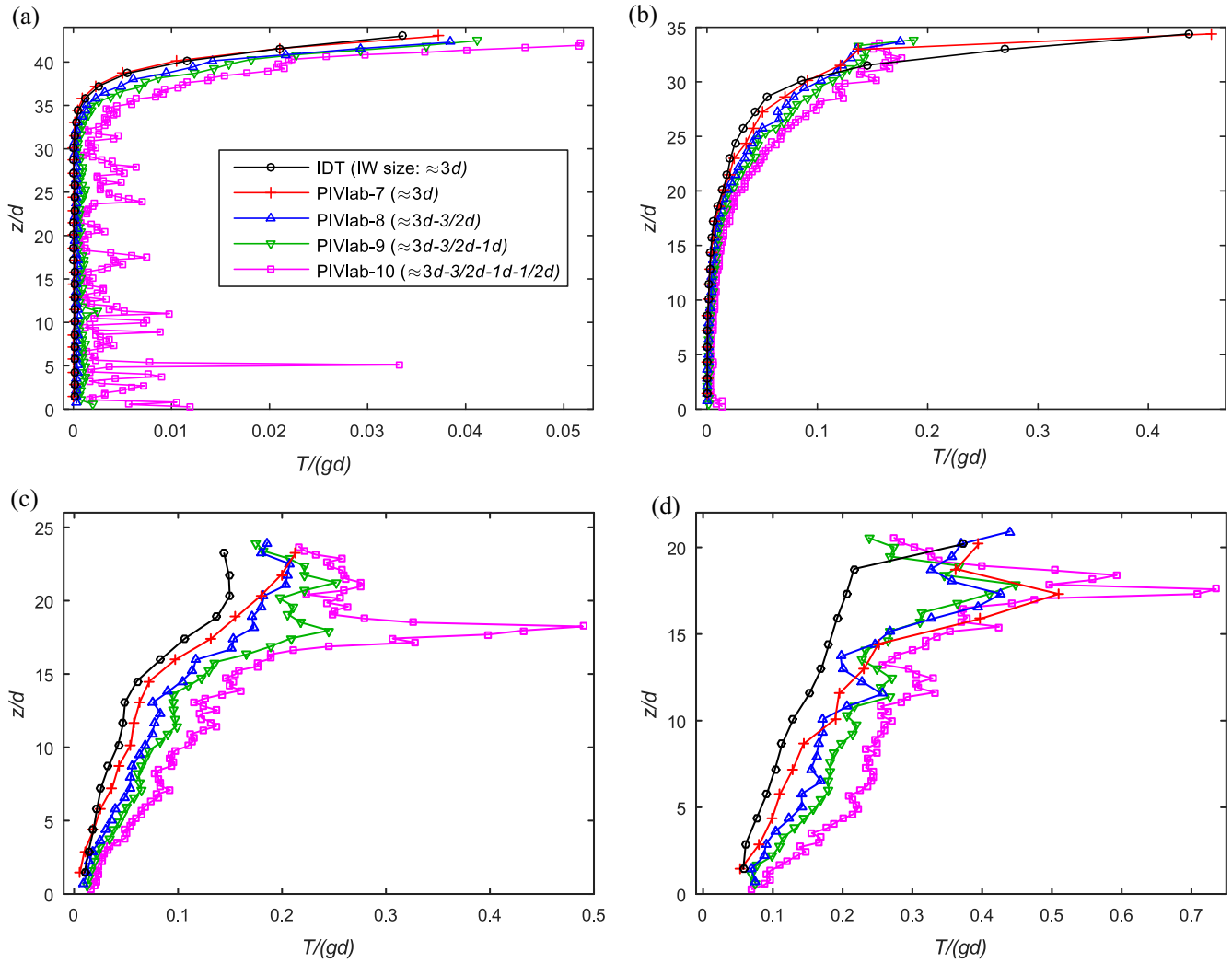

Fig. 8. Profiles of the granular temperature, obtained by different PIV analyses (a) Exp-28, (b) Exp-31, (c) Exp-34, (d) Exp-40.

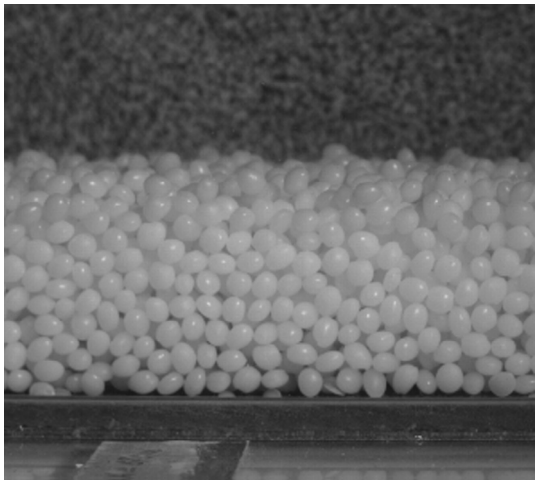

Fig. 9. Picture of the POM material, taken by the high-speed camera AOS S-PRI at the side wall of the flume.

of 30°. Similar to the apparatus of Section 3.2, an upper reservoir is connected to the flume by a 5 cm-high gate, located close to the basal surface. In order to investigate a no-slip KBC, the flume basal surface was lined with a coarse sandpaper (grit P40 FEPA/ISO 6344, avg. particle diameter 425 μm). The instrumentation, slightly different from previous investigations, consisted of a monochrome high-speed camera, mod. AOS S-PRI, capable of video-recording up to 1000 fps with a spatial resolution of 1024 × 1024 pixels and 8-bit pixel depth, and of a flickering-free LED lamp, mod. Photo-Sonics MultiLED-LT (≈8000 lm). The camera, equipped with a lens of focal length 25 mm (mod. Pentax B2514D), was placed aside the flume at a distance of ≈40 cm from the side wall and was centered at the investigated cross section ($x = 0.2$ m downstream the gate). Analogous to the previous experiments, the LED lamp was placed aside the flume at a distance of ≈30 cm. The spatial scale of the images is $1d \approx 15.6$ pixels, corresponding to 1 pixel ≈ 0.212 mm. According to the specifications of the camera, the acquisition frequency was set to 1000 fps, instead of 2000 fps as in the previous investigations. The camera shutter time and the lens aperture were set to 150 μs and $f/4$, respectively. The employed granular material consists of poorly-disperse matte-white spheroidal beads, made of the (POM) acetal copolymer, and exhibit a mean diameter of 3.3 mm, a relative standard deviation of d of 5% [42] and an internal angle of friction ≈27° [37,39]. A picture showing the optical properties of the granular medium is reported in Fig. 9. Neither dye nor different colors of grains were employed here. These more restrictive conditions, together with the fact that the POM beads exhibit weaker sub-grain textures than Ottawa sand, render this test more challenging for PIV. Nonetheless, it can be noted from Fig. 9 that the POM beads are less prone to occasional glares thanks to their matte-reflective surface, which conversely slightly helps the PIV cross-correlation (cf. the autocorrelation analysis in Appendix A).

In the reported experiment, hereafter referred to as Exp-POM-30, 2000 images, taken from a time interval of 2 s within the steady state, were analyzed by PIVlab, so that 1000 instantaneous velocity measurements are obtained. All the PIV analyses are performed on a squared ROI (of size 6 cm), centered at the investigated cross section, while only the velocity measurements at the cross section are subsequently reported. In the investigated time interval the flow depth was found equal to ≈9.5d. Different PIV settings were studied (Table 7). Similar to the investigation in the rotating drum (cf. Section 3.1), the first series of tests (from PIVlab-11 to PIVlab-14) employed a 1st pass IW of size ≈2d (i.e. 32 pixels). As well, in the second series of PIV tests, larger IWs were investigated in the 1st pass: i.e. ≈4d and ≈8d for the tests PIVlab-15 and PIVlab-16, respectively. The time-averaged velocity and granular temperature profiles are reported in Fig. 10, where the inset Fig. 10(b) shows the PIV-estimated velocities closest to the basal surface. First of all, it is evident that all PIV analyses well capture the same approximately linear shape of u_x, which is similar to the u_x profile of Exp-40 involving Ottawa sand. It might be surprising that here, despite the no-slip basal KBC, the PIV estimation nearest to the basal surface is greater than zero. However, as extensively discussed by Sarno et al. [44], this finding is essentially due to basal grains' rolling, made possible by the low roughness of the sandpaper compared to the grain diameter. The u_z profile, which is ≈0 along the flow depth, is equally captured by all PIV tests. Table 7 also shows the runtimes of the various PIV analyses, carried out on the same machine (Intel Core I7-2600@3.40 GHz). As expected, the employment of the multi-pass window deformation method increases the total computation time, due to the additional computational costs of both iterative PIV analyses and interpolation stages of the window deformation algorithm. However, it is worth underlining that such an increase of runtime grows less than linearly with the increment of the PIV spatial resolution achieved in the last pass (e.g. compare the run-times of PIVlab-11, PIVlab-12, PIVlab-13, PIVlab-14, where the IW sizes in the last pass are 32, 16 and 8 pixels respectively).

As expected, Fig. 10(a) and (b) show that also in this case the single pass analysis, PIVlab-11, noticeably underestimates the flow velocities, with the maximum discrepancy being observed closest to the free surface. Moreover, it is confirmed that the estimated flow velocities slightly increase as the IW is refined and rapidly tend to an asymptotic profile. In agreement to that already observed in Section 3.1, it is also confirmed that the employment of a larger IW (PIVlab-15 and PIVlab-16) in the 1st pass yields a slight additional increase of the estimated flow velocities (cf. Fig. 10(b)). Yet, it should be noted that no further improvement (with respect to PIVlab-15) is achieved by using an extremely large 1st pass IW of size ≈8d (PIVlab-16). On the contrary, PIVlab-16 is slightly worse than PIVlab-15, due to the coarser spatial resolution in the last pass. To this regard, it is worth underlining once again that a fine PIV mesh of 1d or even smaller is highly advisable to get reliable velocity measurements at the boundaries of the flow domain and especially near the free surface.

As shown by Fig. 10(c), all the T profiles, obtained by different PIV analyses, basically follow the same trend, where T increases

Table 7
List of the PIV analyses on chute flow of POM beads (Exp-POM-30).

PIV analysis	Employed interrogation windows	Overlap	Run-time [s]
PIVlab-11	Single pass, IW: 32 × 32	16 pixel (i.e. 3.38 mm ≈ 1d)	290
PIVlab-12	Two pass, IWs: 32 × 32, 16 × 16	8 pixel (1.69 mm ≈ 0.5d)	425
PIVlab-13	Three pass, IWs: 32 × 32, 16 × 16, 8 × 8	4 pixel (0.85 mm ≈ 0.25d)	571
PIVlab-14	Four pass, IWs: 32 × 32, 16 × 16, 8 × 8, 4 × 4	2 pixel (0.42 mm ≈ 0.13d)	770
PIVlab-15	Four pass, IWs: 64 × 64, 32 × 32; 16 × 16; 8 × 8	4 pixel (0.85 mm ≈ 0.25d)	688
PIVlab-16	Four pass, IWs: 128 × 128, 64 × 64, 32 × 32; 16 × 16	8 pixel (1.69 mm ≈ 0.5d)	648

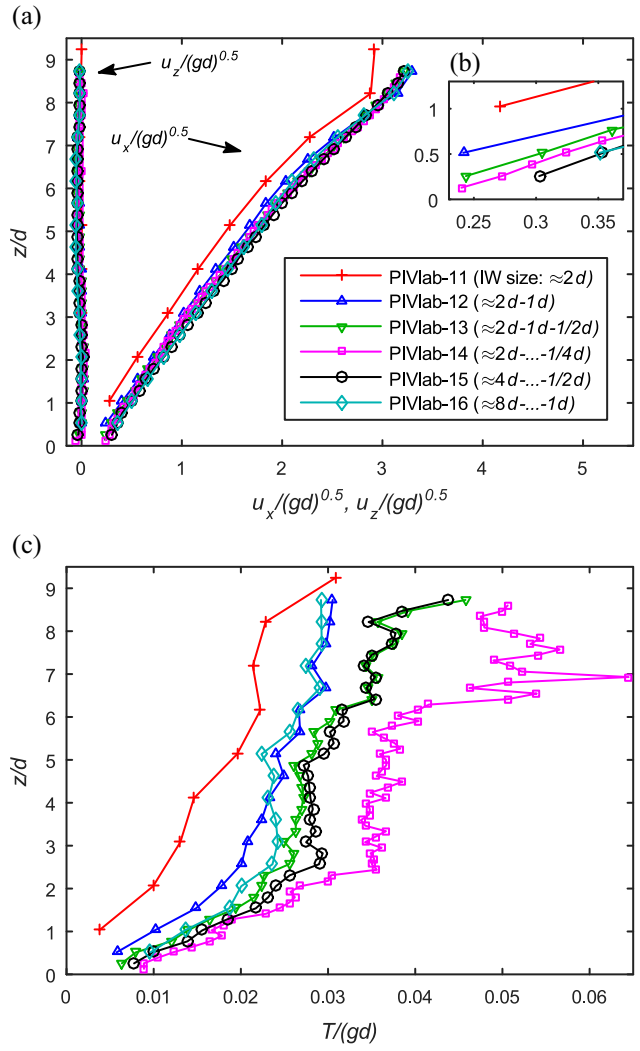

Fig. 10. Sidewall profiles of the chute flow experiment, Exp-POM-30 (a) Time-averaged flow velocities, (b) Inset plot of $(u_x|_{z\approx 0})/(gd)^{0.5}$, (c) Granular temperatures.

with z. Such a trend is analogous to that already observed in the experiments Exp-34 and Exp-40, characterized by similar u_x velocity profiles (cf. Figs. 7 and 8). As expected, the estimated T typically increases, if the last-pass IW is refined. An exception of this trend is represented by the analysis, PIVlab-14, which exhibits a strong increase of T, compared to PIVlab-13, and a jagged noisy profile. In the light of the previous findings, such T estimations appear affected by large random errors, in turn caused by a too small IW in the last pass (4 pixels in this case). Finally, it is interesting to note that the T profiles by PIVlab-12 and PIVlab-16 are very similar and also those ones by PIVlab-13 and PIVlab-15 match each other quite closely. It indicates that the PIV estimation of T is chiefly governed by the IW size in the last pass, while it is much less sensitive to the IW size employed in the 1st pass or to other PIV settings (e.g. the number of PIV passes). These findings, in good agreement with the previous ones, corroborate the reliability of the proposed multi-pass PIV approach and indicate that, even without optical treatments to the grain material (e.g. dye), robust PIV measurements of time-averaged velocities and granular temperature are feasible.

3.4. Scaling of the granular temperature with the PIV resolution

The overall behavior of the estimated granular temperatures, depending on the size of IW in the last pass, is briefly summarized.

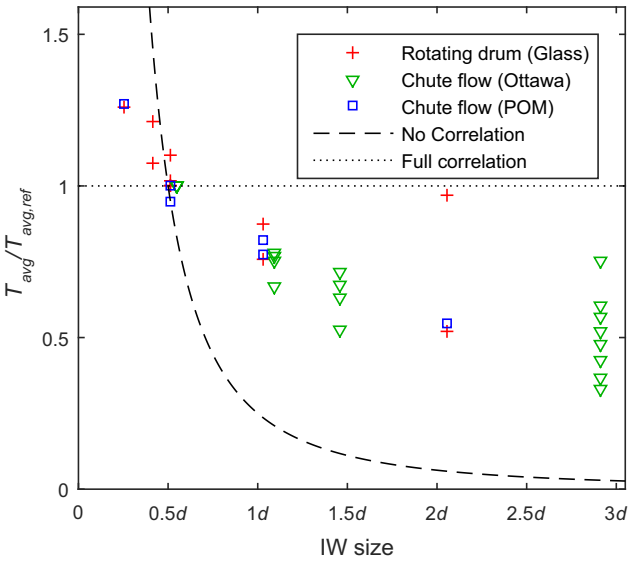

Fig. 11. Normalized depth-averaged granular temperatures versus the size of the last-pass IW.

For each experiment and PIV setting the following depth-averaged granular temperature, T_{avg}, was calculated

$$T_{avg} = \frac{1}{(h-2d-k)} \int_{k}^{h-2d} T(z)dz \tag{7}$$

where k represents the z-coordinate below which $u_x/\sqrt{gd} < 0.1$ (conversely, k is set equal to 0 if $u_x/\sqrt{gd} > 0.1$ everywhere). The cut-off for $z < k$ and $z > (h\text{-}2d)$ is here considered so as to neglect non-significant/unreliable estimations of T, located in the almost static lower region and close to the free surface. In order to compare all T measurements together, each T_{avg} value was normalized by a reference value, $T_{avg,ref}$, chosen equal to the value obtained in the same experiment by using the last-pass IW of size $\approx 1/2d$ (i.e. by analyses PIVlab-3, PIVlab-10 and PIVlab-15 in the three series of experiments). All data were synthetically reported in Fig. 11, in which the x-axis represents the size of the last-pass IW. In Fig. 11 the theoretical curves, obtained under the hypotheses of full and no-spatial correlation of the instantaneous velocities (cf. Section 2), are also reported. Almost all points lie between the two theoretical lines, excepting for few data at the left-hand side of the reference point, corresponding to finer PIV analyses affected by noise. Due to PIV averaging errors, a general decreasing trend of T_{avg} with increasing IW size is observed with a relatively low scatter, which is rather surprising considering the vast heterogeneity of experiments and flow regimes investigated. Yet, as already underlined, such a decrease of T_{avg} is noticeably weaker than that expected under the hypothesis of no-correlation. It suggests that some correlation between contiguous velocity measurements occurs even at length scales much larger than $1d$. As already remarked, this behavior, which merits further investigation from the viewpoint of physics, is clearly beneficial for the accuracy achievable by a PIV approach in estimating the granular temperatures.

4. Conclusions

The multi-pass window deformation 2D-PIV approach to granular flows is investigated by employing the free open-source code PIVlab. Three granular materials (glass spheres, Ottawa sand and POM beads) in two different flow geometries (rotating drum and chute flows) are involved in this study. The effects of the IWs sizes

to PIV estimations are systematically investigated, so that a reliable PIV setting in measuring the time-averaged velocity and granular temperature could be identified. In rotating drum experiments, the controlled rotating speed allowed the assessment of the absolute accuracy of PIVlab. The minimum errors near the basal surface (≈0.01–0.06 pixel/frame), obtained by using the best PIV setting (i.e. 4 passes and IW sizes of ≈4*d*-2*d*-1*d*-1/2*d*), are found only slightly larger than the PIVlab random error under ideal conditions (≈0.02 pixel/frame). Conversely, much larger errors arise in case of sub-optimal PIV settings. In chute flows of Ottawa sand, the commercial code IDT ProVision-XS and PIVlab, operated with identical settings (i.e. single-pass mode), yield comparable estimations of time-averaged velocities and granular temperatures. Yet, when more than one PIV pass is employed, PIVlab appears to provide superior results in terms of both accuracy and spatial resolution. While in the first two campaigns specific pretreatments were undertaken for enhancing the grains' optical properties, the investigation on POM beads, where no pretreatment was employed, provides further evidence of the robustness of the proposed multi-pass PIV approach. In this third experimental campaign, the computational costs of the multi-pass window deformation approach are also briefly reported. It emerges that the runtime overheads appear more than compensated by the increased quality and resolution of measurements.

A clear and unique trend is observed in all experiments. Owing to PIV spatial averages, the coarser the IW in the last pass, the larger is the underestimation of both time-averaged velocities and granular temperatures. Thus, the critical importance of a high spatial refinement (of order of ≈1*d* or finer), which can be straightforwardly achieved by the multi-pass approach, clearly emerged. As well, it is observed that a sufficiently large 1st pass IW, encompassing a minimum number of grains, is crucial to get the most accurate estimation of the flow velocities. Thanks to the optical texture of the granular material, the optimal size of the 1st pass IW is found to be ≈3*d*-4*d*, while an even larger IW is unnecessary. Therefore, in the context of g-PIV this minimum requirement for the size of the 1st pass IW substitutes the classical 2D-PIV rule of ensuring a tracer density of 5–10 per IW. Conversely, this requirement is typically more restrictive than the classical guideline for avoiding loss-of-pair issues, which prescribes a IW ≈4x larger than the maximum displacement.

The PIV estimations of the granular temperature, *T*, are in substantial agreement with the theory by Reynolds et al. [34] where finer PIV analyses are expected to better approximate the true local value of *T*, by yielding progressively larger estimations. Yet, the rate of increase of *T* estimations is found to be much lower than that theoretically expected by assuming fully uncorrelated instantaneous velocities. It indicates the existence of strong spatial correlations among contiguous instantaneous velocities. While on length scales up to ≈1*d* the correlations of grains with themselves are expected to be relevant [34], on length scales larger than 1*d*, grains' correlated motion, depending on non-local dissipation mechanisms, probably arise. Clearly, both correlations mechanisms are beneficial for the estimation of *T* by the multi-pass PIV approach, which appears reliable as long as the spatial refinement is equal or finer than ≈1*d*. Finally, noticeable noise of *T* profiles is systematically observed, when the size of the last-pass IW becomes smaller than few pixels. Such a noise is caused by the deterioration of the PIV cross-correlation due to the limited resolution of the camera sensor. In the whole investigated dataset a lower limit for the PIV refinement is found to be equal to ≈6–7 pixels. Remarkably, such a limit is not only independent from the size and optical properties of the granular medium but also from the flow dynamics.

In the light of all above considerations a general guideline for g-PIV applications emerges. Reliable PIV estimations appear achievable by fully employing the PIVlab multi-pass capabilities and IW sizes of ≈4*d*-2*d*-1*d*-1/2*d*, provided that the aforementioned requirements about loss-of-pair issues and the minimum size of the last-pass IW in terms of pixels are fulfilled.

Acknowledgements

The first two experimental campaigns were conducted during the first author's PhD training granted by the University of Napoli "Federico II". The authors wish to thank Prof. I. C. Liu for the experiments with the rotating drum carried out at the National Chi Nan University (Taiwan). As well, Ing. Nicola Immediata is acknowledged for assistance in the experimental design at the University of Salerno (Italy). Moreover, the authors wish to thank the anonymous reviewers for their valuable suggestions to improve the quality of the paper.

Appendix A

In this appendix we report autocorrelation image tests on granular materials, useful for assessing the suitability of the Gaussian sub-pixel interpolation in g-PIV applications. Auto-correlation analyses, using images of size 60 × 60 pixels of the three investigated granular materials, are performed. To illustrate the appropriateness of the Gaussian interpolation algorithm, it was convenient that the three investigated images had slightly different spatial scales and the third one was even obtained by using a different acquisition system. Each image is correlated with itself, so that the correlation function corresponds to the ideal case of a cross-correlation between the original image and an image with the same noise pattern and null relative displacement $(s_x, s_y) = (0, 0)$. In this way, without loss of generality we could evaluate the shape of the peak as a function of the sole optical properties of the granular material (grain shape, sub-grain texture etc..) and of the acquisition system. As shown by Fig. A1, for all granular media the normalized autocorrelation function, $C(s_x, s_y)$, exhibits a typical normal behavior around the peak at $(s_x, s_y) = (0, 0)$. To fit $C(s_x, s_y)$, we use the 2D Gaussian function

$$f(s_x, s_y) = \exp\left(-\left(\frac{{s_x}^2}{2\sigma_x^2} + \frac{{s_y}^2}{2\sigma_y^2}\right)\right) \tag{A1}$$

where σ_x and σ_y are the standard deviations of f in the x- and y-directions.

Table A1 lists the Gaussian best-fits related to the image samples of Fig. A1, obtained by considering 9-point (3 × 3) and 25-point (5 × 5) regressions around the peak. As expected, R^2 is highest in the case of the 9-point regression, which involves a lower number of points. When the stencil of the regression enlarges, a decrease of R^2 is observed, since the auto-correlation function is generally higher than the Gaussian function at increasing distances from the peak. This is probably due to some recurrence of the granular pattern, which causes relatively higher values of the auto-correlation function, *C*, in regions far from the peak. Nonetheless, discrepancies far from the peak between the autocorrelation function and the Gaussian fit are irrelevant for the typical employment of Gaussian sub-pixel algorithms, like the ones implemented in PIVlab, which only use 6 (in the 2 × 3 - point version) or 9 data points (in the 2D version). For each auto-correlation analysis, the standard deviations, σ_x and σ_y, are of the same order, indicating that the image pattern is roughly isotropic. It could be also noted that the peak in the first image (Fig. A1 (a)) is wider than the other two cases (Fig. A1(b)–(c)). This finding is congruent with the poorer sub-grain texture of the glass beads, compared to the other investigated granular materials. With this

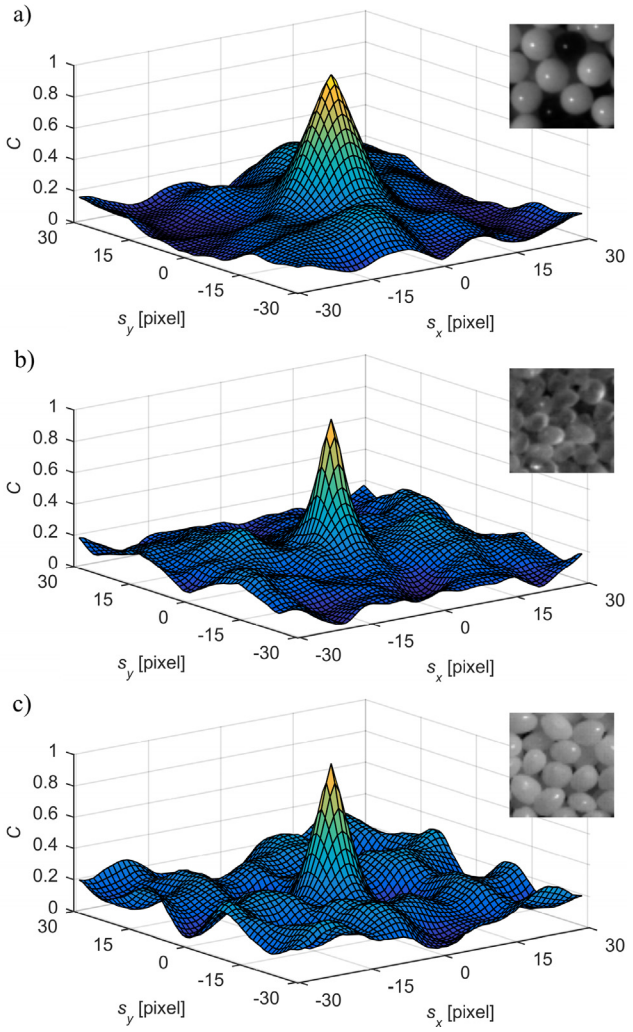

Fig. A1. Normalized auto-correlation function (sample image of size 60×60 pixels): (a) glass beads, (b) Ottawa sand, (c) POM beads.

Table A1
Parameters of the Gaussian best-fits.

Granular medium	Regression type	σ_x [px]	σ_y [px]	R^2
Glass beads	9-point	3.33	3.04	0.99
Glass beads	25-point	3.87	3.69	0.94
Ottawa sand	9-point	2.21	2.20	0.99
Ottawa sand	25-point	2.48	2.61	0.94
POM beads	9-point	2.13	2.12	0.97
POM beads	25-point	2.56	2.62	0.88

brief investigation, we conclude that a Gaussian fit appears generally suitable for obtaining sub-pixel accuracy also in g-PIV applications.

Appendix B

In this appendix the fitness of the 3*d*-IW-size criterion for the first-pass calculation in g-PIV is demonstrated. The tests are performed using three PIV sample image pairs of size 250×250pixels for the three granular media (Fig. B1). Such image pairs can be viewed as semi-synthetic, since the second images are constructed by shifting the first images vertically by a known displacement, s_y, while the horizontal displacement is kept null (i.e. $s_x = 0$). The IW

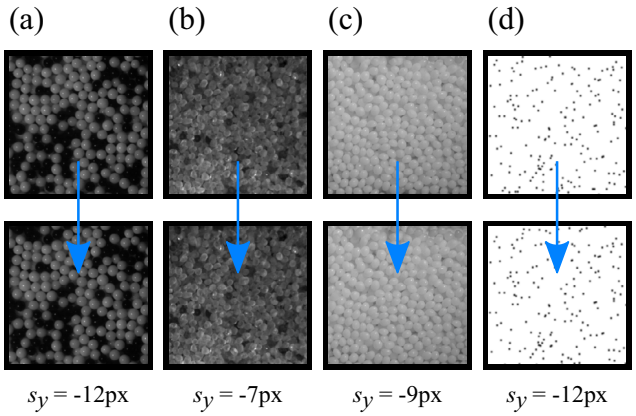

Fig. B1. Image pairs. (a) glass beads, (b) Ottawa sand, (c) POM beads, (d) synthetic round-shaped seeders (spatial density of 0.0028 seeders per pixel).

size in the first pass is $\approx 3d$, while the vertical shift of the second image is chosen equal to $0.6d$ (i.e. $\approx 1/5$ of the IW size in the first pass), so that we could easily compare PIV analyses on different granular materials. A 50% overlap is employed for all PIV analyses. Owing to different spatial scales of images and different grain sizes, the 3*d* IW size in the first-pass is set equal to 60 pixels, 32 pixels and 48 pixels for the glass beads, Ottawa sand and POM beads samples, respectively, while the vertical displacements (approximated to the nearest integer) are 12 pixels, 7 pixels and 9 pixels. It was also verified that smaller displacements yield errors comparable or smaller than those here reported. Different numbers of PIV passes were investigated. For each PIV analysis, the velocities, obtained from different IWs, are spatially averaged over the whole image. As well, for each IW the peak ratio (i.e. the ratio between the highest and the second peak), which is a rough indicator of the robustness of the PIV correlation analysis, could be calculated at each PIV pass and is subsequently averaged over the entire image (only cross-correlation maps exhibiting a second peak are considered in the calculation of this average).

In order to compare the effects on PIV of the grain texture with those of the seeders in classical 2D-PIV, additional PIV analyses on a fully synthetic frame pair (Fig. B1(d)) are reported. In the fashion of the classical PIV applications, the first image (size 250×250 pixels, 8-bit pixel depth) is built up by randomly adding round-shaped seeders (diameter $D = 3$ pixels, Gaussian intensity distribution with $\sigma = 1$ pixel) in a blank image. The seeders' density is 0.0028 seeders per pixel, so that ≈ 10 seeders are contained in a IW of size 60 pixels. The second image is obtained by vertically shifting the first image by 12 pixels. All the PIV results are listed in Table B1, where the PIV estimations of the horizontal and vertical displacements are represented by the symbols $\hat{s}_x$ and $\hat{s}_y$, so as to distinguish them from the actual displacements, s_x and s_y.

As shown by Table B1, the employment of a greater number of PIV passes systematically yields lower displacement errors. For all granular media, the error on the horizontal displacement, $\hat{s}_x$, is much lower (typically $\ll 0.02$ pixel/frame) than that on the vertical displacement, $\hat{s}_y - s_y$. Conversely, while for the fully synthetic images (Fig. B1(d)) an error on the vertical displacement of order of 0.02 pixel/frame is achieved even by the 2-pass analysis, for granular media only a complete four-pass PIV analysis is capable of yielding comparably accurate results. Slightly larger errors ($\approx$0.05 pixel/frame) are observed in the case of glass beads. In this case the lower accuracy might be due to recurrent grain patterns within the same IW, which cannot be properly counterbalanced by the weak sub-grain texture of the glossy granular material.

The peak ratio is generally ≥ 2 for all passes regardless the type of granular medium, while it is only marginally smaller than that

Table B1
PIV analyses on semi-synthetic and synthetic image pairs ($s_x = 0$ for all tests).

Granular medium	PIV analysis	Peak ratio in the last PIV pass	$\hat{s}_x$ [px]	$\hat{s}_y$ [px]	s_y [px]
Glass beads	Single pass, IW: 60 × 60	1.992	−0.059	−11.738	−12
Glass beads	Two pass, IWs: 60 × 60, 30 × 30	2.455	−0.021	−11.871	−12
Glass beads	Three pass, IWs, 60 × 60, 30 × 30, 15 × 15	3.342	−0.010	−11.912	−12
Glass beads	Four pass, IWs: 60 × 60, 30 × 30, 15 × 15, 8 × 8	3.279	−0.004	−11.949	−12
Ottawa sand	Single pass, IW: 32 × 32	2.346	0.028	−6.812	−7
Ottawa sand	Two pass, IWs: 32 × 32, 16 × 16	2.740	0.008	−6.915	−7
Ottawa sand	Three pass, IWs, 32 × 32, 16 × 16, 12 × 12	2.832	0.005	−6.949	−7
Ottawa sand	Four pass, IWs: 32 × 32, 16 × 16, 12 × 12, 6 × 6	2.025	0.003	−6.966	−7
POM beads	Single pass, IW: 32 × 32	2.009	−0.004	−8.917	−9
POM beads	Two pass, IWs: 32 × 32, 16 × 16	2.517	0.001	−8.958	−9
POM beads	Three pass, IWs, 32 × 32, 16 × 16, 12 × 12	2.862	0.002	−8.972	−9
POM beads	Four pass, IWs: 32 × 32, 16 × 16, 12 × 12, 6 × 6	2.000	0.001	−8.979	−9
Synthetic seeders	Single pass, IW: 60 × 60	2.748	−0.001	−11.925	−12
Synthetic seeders	Two pass, IWs: 60 × 60, 30 × 30	2.909	−0.002	−11.978	−12
Synthetic seeders	Three pass, IWs, 60 × 60, 30 × 30, 15 × 15	3.364	−0.003	−12.000	−12
Synthetic seeders	Four pass, IWs: 60 × 60, 30 × 30, 15 × 15, 8 × 8	3.287	−0.005	−12.004	−12

observed in the case of synthetic seeders (>2.5). Typically, the peak ratios increase in subsequent PIV passes, indicating that the possible losses of accuracy/rounding errors due to the additional PIV calculations are more than counterbalanced by the advantages of the multi-pass approach. Congruent with that already observed as regards the displacement errors, the average peak ratios for the glass beads and for POM beads are slightly smaller than those observed for the case of Ottawa sand, which reflects the relatively poorer sub-grain optical texture of these materials.

This complementary investigation indicates that a g-PIV analysis with a first-pass IW of size 3*d* and a suitable refinement in the subsequent passes is generally capable of providing robust results, which are also comparable with those obtainable by employing a seeder density of ≈10 per IW in classical 2D-PIV applications.

Appendix C

The statistical approach by Reynolds et al. [34] for assessing the bounds, between which the PIV estimation of the granular temperature varies with the size of the interrogation window, is concisely reported here. Let us consider a velocity field $\boldsymbol{u}(\boldsymbol{x}, t)$ varying in space $\boldsymbol{x}$ and time t. For the sake of simplicity, the subsequent calculations will be derived for a uniform flow, where the sole x-component $u_x(\boldsymbol{x}, t)$ is non-null. Analogous considerations also hold for three-dimensional flows. Let us assume that the velocity field is discretized in M spatial sub-regions ($u_{x,1}$, $u_{x,2} \ldots$, $u_{x,M}$) per unit area, and K time points (i.e. in any i-th spatial sub-region several measurements are taken at different times $u_{x,i}(t_1)$, $u_{x,i}(t_2), \ldots, u_{x,i}(t_K)$). For each i-th spatial sub-region the following statistics can be written

$$\bar{u}_{x,i} = \frac{1}{K}\sum_{k=1}^{K} u_{x,i}(t_k) = E\left[u_{x,i}\right] \tag{C1}$$

$$\sigma_i^2 = \frac{1}{K}\sum_{k=1}^{K}\left(u_{x,i}(t_k) - \bar{u}_{x,i}\right)^2 = E\left[\left(u_{x,i} - \bar{u}_{x,i}\right)^2\right] \tag{C2}$$

$$\begin{aligned}\sigma_{i,j} &= \frac{1}{K}\sum_{k=1}^{K}\left(u_{x,i}(t_k) - \bar{u}_{x,i}\right)\left(u_{x,j}(t_k) - \bar{u}_{x,j}\right)\\ &= E\left[\left(u_{x,i} - \bar{u}_{x,i}\right)\left(u_{x,j} - \bar{u}_{x,j}\right)\right]\end{aligned} \tag{C3}$$

where the symbol $E[\ ]$ represents the mathematical expectation operator. The first quantity, $\bar{u}_{x,i}$, is the time-average; the second one, σ_i^2, is the second-order statistics, i.e. the variance of $u_{x,i}(t)$ in the investigated time interval, while $\sigma_{i,j}$ is the covariance between the flow velocities measured in two different spatial regions i and j. The correlation function is defined as $\rho_{i,j} = \sigma_{i,j}/(\sigma_i\sigma_j)$. Assuming spatial homoscedasticity, it follows that $\sigma_1 = \sigma_2 = \ldots = \sigma_M$. By assuming also the ergodicity of the process, the estimated granular temperature at any i-th sub-region, is given by

$$T_i = \left\langle \left(u'_{x,i}\right)^2 \right\rangle \approx \sigma_i^2 = \sigma_1^2 = \sigma_2^2 = \ldots = \sigma_M^2. \tag{C4}$$

Clearly $T = T(M)$ is function of the size of the spatial sub-regions and, consequently, of their number, M, per unit area. In fact, the coarser is the spatial discretization the more the estimated instantaneous velocities, $u_{x,i}(t)$, are dampened by the spatial average, which acts as a low-pass filter. If the spatial resolution M is high enough compared to the size of the grain particles, $T(M)$ tends to the true local value of the granular temperature. Thanks to Eq. (C4), the correlation function, $\rho_{i,j}$, can be rewritten as $\rho_{i,j} = \sigma_{i,j}/T(M)$.

Considering now a unique spatial region containing all the M sub-regions, any velocity measurement at any time-point t_j can be merely calculated as the average of the M previous velocities, $u_x(t_j) = (u_{x,1}(t_j) + u_{x,2}(t_j) + \ldots + u_{x,M}(t_j))/M$. By using Eqs. (C1)–(C3), the statistics related to this larger spatial region can be written as

$$\bar{u}_x = \frac{1}{M}\sum_{i=1}^{M}\bar{u}_{x,i} = E\left[\frac{1}{M}\left(u_{x,1} + u_{x,2} + \ldots + u_{x,M}\right)\right] \tag{C5}$$

$$\begin{aligned}T(1) = \sigma^2 &= \tfrac{1}{K}\sum_{k=1}^{K}\left(u_x(t_k) - \bar{u}_x\right)^2 = E\left[\left(\tfrac{1}{M}\left(u_{x,1} + u_{x,2} + \ldots + u_{x,M}\right) - \bar{u}_x\right)^2\right]\\ &= \tfrac{1}{M^2}\left(\sum_{i=1}^{M}\sigma_i^2 + 2\sum_{i=1}^{M}\sum_{j>i}^{M}\sigma_{ij}\right) = \tfrac{1}{M^2}\left(M\,T(M) + 2\sum_{i=1}^{M}\sum_{j>i}^{M}\rho_{ij}T(M)\right)\\ &= \tfrac{T(M)}{M^2}\left(\sum_{i=1}^{M}\sum_{j}^{M}\rho_{i,j}\right),\end{aligned} \tag{C6}$$

where $1/M$ clearly is the ratio between the area of the former finer spatial discretization and that of the latter coarser one. Eq. (C6) quantitatively relates the granular temperatures, calculated by PIV on different spatial discretizations. From (C6) it follows that $T(A) \leqslant T(B)$, if $A < B$, i.e. as the grid is refined. In the ideal case of no spatial correlation between measurements in the M contiguous sub-regions,

$$\rho_{i,j} = \begin{cases} 1 & i = j \\ 0 & i \neq j \end{cases} \tag{C7}$$

therefore, a linear relationship holds: $T(1) = (1/M)T(M)$. Conversely, in the other limiting case of full spatial correlation, $\rho_{i,j} = 1$ for any (i,j) and, consequently, $T(1) = T(M)$. In real granular flows the estimated T scales as a function of the PIV spatial resolution somewhere between these two limiting conditions, depending on the term $\sum_{i=1}^{M}\sum_{j}^{M}\rho_{i,j}$, which, however, cannot be evaluated *a priori*. In fact, the magnitude of spatial correlations of the flow velocity and their length scale may depend on the flow dynamics. In the quasi-static and dense-collisional regimes the length scale of such correlations could be larger than one particle diameter (e.g. [24,32]); conversely, in a purely collisional flow the motion of grains is expected to be chiefly uncorrelated. However, even if the velocity fluctuations of distinct grain particles are completely uncorrelated, there is always some correlation between contiguous IWs. In fact, as underlined by Reynolds et al. [34], the motion of the same particle might be detected in contiguous interrogation windows, which implies some degree of correlation among contiguous PIV measurements. Based on purely geometrical arguments, Reynolds et al. [34] showed that the correlation function of a perfectly circular particle (of diameter d) with itself rapidly drops to 0 for distances greater than $1d$ and can be roughly approximated by a linearly decreasing function, $\rho(s) \approx 1 - s/d$, of the separation s from the particle.

References

[1] R.J. Adrian, Twenty years of particle image velocimetry, Exp. Fluids 39 (2) (2005) 159–169.
[2] R.J. Adrian, J. Westerweel, Particle Image Velocimetry (No. 30), Cambridge University Press, 2011.
[3] S. Albaraki, S.J. Antony, How does internal angle of hoppers affect granular flow? Experimental studies using digital particle image velocimetry, Powder Technol. 268 (2014) 253–260.
[4] T. Astarita, G. Cardone, Analysis of interpolation schemes for image deformation methods in PIV, Exp. fluids 38 (2) (2005) 233–243.
[5] J.L. Baker, T. Barker, J.M.N.T. Gray, A two-dimensional depth averaged (I)-rheology for dense granular avalanches, J. Fluid Mech. 787 (2016) 367–395.
[6] H. Capart, D.L. Young, Y. Zech, Voronoï imaging methods for the measurement of granular flows, Exp. Fluids 32 (1) (2002) 121–135.
[7] J.J. Charonko, P.P. Vlachos, Estimation of uncertainty bounds for individual particle image velocimetry measurements from cross-correlation peak ratio, Meas. Sci. Technol. 24 (6) (2013) 065301.
[8] Z. Chen, C. Jiang, H. Nepf, Flow adjustment at the leading edge of a submerged aquatic canopy, Water Res. Res. 49 (9) (2013) 5537–5551.
[9] S.H. Chou, H.J. Hu, S.S. Hsiau, Investigation of friction effect on granular dynamic behavior in a rotating drum, Adv. Powder Tech. 27 (5) (2016) 1912–1921.
[10] H.-T. Chou, C.-F. Lee, Cross-sectional and axial flow characteristics of dry granular material in rotating drums, Granul. Matter 11 (1) (2009) 13–32.
[11] W. Eckart, J.M.N.T. Gray, K. Hutter, Particle Image Velocimetry (PIV) for granular avalanches on inclined planes, in: K. Hutter, N. Kirchner (Eds.), Lecture Notes in Applied & Computational Mechanics (Vol. 11), Dynamic Response of Granular and Porous Materials Under Large Catastrophic Deformations, Springer, 2003, pp. 195–218.
[12] G. Elsinga, F. Scarano, B. Wieneke, B. van Oudheusden, Tomographic particle image velocimetry, Exp. Fluids 41 (2006) 933–947.
[13] T. Fahringer, K. Lynch, B. Thurow, Volumetric particle image velocimetry with a single plenoptic camera, Meas. Sci. Technol. 26 (2015) 115201.
[14] G.D.R. Midi, On dense granular flows, Eur. Phys. J.E Soft. Matter. 14 (4) (2004) 341–365.
[15] D. Gollin, W. Brevis, E.T. Bowman, P. Shepley, Performance of PIV and PTV for granular flow measurements, Granul. Matter 19 (3) (2017) 42.
[16] IDT VISION, 2011. User Manual, ProVISION-XS, Software release 3. 11.
[17] Z.K. Jahanger, S.J. Antony, J. Richter, Displacement patterns beneath a rigid beam indenting on layered soil, in: Pro. Eighth Amer. Reg. Conf. Int. Soc. Terrain Vehicle Sys. Michigan, USA, Paper No. 67, 2016.
[18] Z.K. Jahanger, J. Sujatha, S.J. Antony, Local and global granular mechanical characteristics of grain–structure interactions, Indian Geotech. J. (2018) 1–15
[19] Z.K. Jahanger, S.J. Antony, E. Martin, L. Richter, Interaction of a rigid beam resting on a strong granular layer overlying weak granular soil: multi-methodological investigations, J. Terramech. 79 (2018) 23–32.
[20] N. Jesuthasan, B.R. Baliga, S.B. Savage, Use of particle tracking velocimetry for measurements of granular flows: review and application, KONA Powder Part. J. 24 (2006) 15–26.
[21] Y.-J. Jiang, I. Towhata, Experimental study of dry granular flow and impact behavior against a rigid retaining wall, Rock Mech. Rock Eng. 46 (4) (2013) 713–729.
[22] P. Jop, Y. Forterre, O. Pouliquen, Crucial role of sidewalls in granular surface flows: consequences for the rheology, J. Fluid Mech. 541 (2005) 167–192.
[23] R.D. Keane, R.J. Adrian, Theory of cross-correlation analysis of PIV images, Appl. Sci. Res. 49 (3) (1992) 191–215.
[24] T.S. Komatsu, S. Inagaki, N. Nakagawa, S. Nasuno, Creep motion in a granular pile exhibiting steady surface flow, Phys. Rev. Lett. 86 (9) (2001) 1757.
[25] S. Lanzoni, C. Gregoretti, L.M. Stancanelli, Coarse-grained debris flow dynamics on erodible beds, J. Geophys. Res. Earth Surf. 122 (3) (2017) 592–614.
[26] R.M. Lueptow, A. Akonur, T. Shinbrot, PIV for granular flows, Exp. Fluids 28 (2) (2000) 183–186.
[27] A.W. Mackowski, C.H.K. Williamson, Direct measurement of thrust and efficiency of an airfoil undergoing pure pitching, J. Fluid Mech. 765 (2015) 524–543.
[28] J.E. Maneval, K.M. Hill, B.E. Smith, A. Caprihan, E. Fukushima, Effects of end wall friction in rotating cylinder granular flow experiments, Granul. Matter 7 (4) (2005) 199–202.
[29] R.M. Nedderman, U. Tüzün, S.B. Savage, G.T. Houlsby, The flow of granular materials - I: Discharge rates from hoppers, Chem. Eng. Sci. 37 (11) (1982) 1597–1609.
[30] M. Ostendorf, J. Schwedes, Application of particle image velocimetry for velocity measurements during silo discharge, Powder Technol. 158 (1–3) (2005) 69–75.
[31] M.N. Papa, L. Sarno, F.S. Vitiello, V. Medina, Application of the 2D Depth-Averaged Model, FLATModel, to Pumiceous Debris Flows in the Amalfi Coast, Water 10 (9) (2018) 1159, https://doi.org/10.3390/w10091159.
[32] O. Pouliquen, Velocity correlations in dense granular flows, Phys. Rev. Lett. 93 (24) (2004) 248001.
[33] S.P. Pudasaini, K. Hutter, S.-S. Hsiau, S.-C. Tai, Y. Wang, R. Katzenbach, Rapid flow of dry granular materials down inclined chutes impinging on rigid walls, Phys. Fluids 19 (5) (2007) 053302.
[34] G.K. Reynolds, A.M. Nilpawar, A.D. Salman, M.J. Hounslow, Direct measurement of surface granular temperature in a high shear granulator, Powder Tech. 182 (2) (2008) 211–217.
[35] S. Roman, C. Soulaine, M.A. AlSaud, A. Kovscek, H. Tchelepi, Particle velocimetry analysis of immiscible two-phase flow in micromodels, Adv. Water Resour. 95 (2016) 199–211.
[36] L. Sarno, R. Martino, M. N. Papa, Discussion of "Uniform Flow of Modified Bingham Fluids in Narrow Cross Sections" by Alessandro Cantelli. J. Hydraul. Eng., 137(5) (2011) 621–621.
[37] L. Sarno, M.N. Papa, R. Martino, Dam-break flows of dry granular material on gentle slopes, in: R. Genevois, D.L. Hamilton, A. Prestininzi (Eds.), 5th Int. Conf. on Debris-Flow Hazards Mitigation: Mechanics, Prediction and Assessment, University of Rome La Sapienza, 2011, pp. 503–512.
[38] L. Sarno, Depth-averaged models for dry granular flows, Phd Thesis, University of Napoli Federico II (Italy), 2013.
[39] L. Sarno, A. Carravetta, R. Martino, Y.-C. Tai, Pressure coefficient in dam-break flows of dry granular matter, J. Hydraul. Eng. 139 (11) (2013) 1126–1133.
[40] L. Sarno, M.N. Papa, Y.C. Tai, A. Carravetta, R. Martino, A reliable PIV approach for measuring velocity profiles of highly sheared granular flows, in: Proc. of 7h WSEAS International Conference on Engineering Mechanics, Structures, Engineering Geology (EMESEG'14), Salerno (Italy), 2014, pp. 134–141.
[41] L. Sarno, A. Carravetta, R. Martino, Y.C. Tai, A two-layer depth-averaged approach to describe the regime stratification in collapses of dry granular columns, Phys. Fluids 26 (10) (2014) 103303.
[42] L. Sarno, M.N. Papa, P. Villani, Y.C. Tai, An optical method for measuring the near-wall volume fraction in granular dispersions, Granul. Matter 18 (4) (2016) 80.
[43] L. Sarno, A. Carravetta, R. Martino, M.N. Papa, Y.C. Tai, Some considerations on numerical schemes for treating hyperbolicity issues in two-layer models, Adv. Water Resour. 100 (2017) 183–198.
[44] L. Sarno, L. Carleo, M.N. Papa, P. Villani, Experimental investigation on the effects of the fixed boundaries in channelized dry granular flows, Rock. Mech. Rock Eng 51 (2018) 203–225.
[45] F. Scarano, M.L. Riethmuller, Iterative multigrid approach in PIV image processing with discrete window offset, Exp. Fluids 26 (1999) 513–523.
[46] F. Scarano, M.L. Riethmuller, Advances in iterative multigrid PIV image processing, Exp. Fluids 29 (1) (2000) S051–S60.
[47] L.-T. Sheng, C.-Y. Kuo, Y.-C. Tai, S.-S. Hsiau, Indirect measurements of streamwise solid fraction variations of granular flows accelerating down a smooth rectangular chute, Exp. Fluids 51 (5) (2011) 1329–1342.
[48] I. Sielamowicz, M. Czech, T.A. Kowalewski, Empirical analysis of eccentric flow registered by the DPIV technique inside a silo model, Powder Technol. 212 (1) (2011) 38–56.
[49] S. Shi, J. Ding, T.H. New, J. Soria, Light-field camera-based 3D volumetric particle image velocimetry with dense ray tracing reconstruction technique, Exp Fluids 58 (2017) 78.
[50] S. Shi, J. Ding, C. Atkinson, J. Soria, T.H. New, A detailed comparison of single-camera light-field PIV and tomographic PIV, Exp Fluids 59 (2018) 46.
[51] Y.C Tai., C.Y. Kuo, A new model of granular flows over general topography with erosion and deposition, Acta Mech. 199(1–4) (2008) 71–96.
[52] W. Thielicke, The Flapping Flight of Birds – Analysis and Application. Phd Thesis, Rijksuniversiteit Groningen, 2014 <http://irs.ub.rug.nl/ppn/382783069>.
[53] W. Thielicke, E. Stamhuis, PIVlab–towards user-friendly, affordable and accurate digital particle image velocimetry in MATLAB, J. Open Res. Soft. 2 (1) (2014).

[54] W. Thielicke, E.J. , PIVlab – Time-Resolved Digital Particle Image Velocimetry Tool for MATLAB (version: 1.41), 2014 <https://doi.org/10.6084/m9.figshare.1092508>.
[55] J. Westerweel, Digital Particle Image Velocimetry-Theory and Application, Ph. D. thesis, Delft University of Technology, the Netherlands, 1993.
[56] J. Westerweel, D. Dabiri, M. Gharib, The effect of a discrete window offset on the accuracy of cross-correlation analysis of digital PIV recordings, Exp. Fluids 23 (1997) 20–28.
[57] D.J. White, W. Take, M.D. Bolton, Soil deformation measurement using particle image velocimetry (PIV) and photogrammetry, Géotechnique 53 (7) (2003) 619–631.
[58] C.E. Willert, M. Gharib, Digital particle image velocimetry, Exp. Fluids 10 (4) (1991) 181–193.